PERGAMON

International Journal of Solids and Structures 36 (1999) 3293–3337

INTERNATIONAL JOURNAL OF SOLIDS and STRUCTURES

Dynamic brittle fracture of high strength structural steels under conditions of plane strain

Youngseog Lee, Vikas Prakash*

Department of Mechanical and Aerospace Engineering, Case Western Reserve University, Cleveland, OH-44106, U.S.A.

Received 2 July 1997; in revised form 29 April 1998

Abstract

A transient finite element analysis is carried out to provide a perspective on dynamic fracture models incorporating the decohesion of fracture surfaces, with a focus on improved modeling and understanding quantitative features of dynamically propagating cracks under intense stress pulse loading. The problem analyzed here is plane-strain fracture of an edge cracked specimen under plane wave loading conditions. In order to ascertain the validity of the various cohesive surface fracture models, the results of the FEM simulations are compared with experimental observations made during the low temperature, plate-impact fracture experiments on 4340VAR steel (200°C temper, $R_c = 55$). The finite element analysis is carried out within a framework where the continuum is characterized by two constitutive relations; one that relates stress and strain in the bulk material, the other relates the traction and separation across a specified set of cohesive surfaces. The bulk material is characterized as an isotropically hardening and thermally softening elastic–viscoplastic von Mises solid. The finite element formulation employed, accounts for the effects of finite geometry changes, material inertia, and heat conduction. Crack initiation and crack growth emerge naturally as outcomes of the imposed loading, and are calculated directly in terms of the material's constitutive parameters and the parameters characterizing the cohesive surface separation law. From the results of these simulations it is observed that the cohesive surface model, which incudes a cohesive surface strength and a characteristic length is not capable of predicting the dynamic crack growth observed in the experiments. However, the computed results are observed to be in good agreement with the experimental results when the work of separation per unit area appearing in the cohesive surface separating law, includes a cohesive-surface separation rate dependent cohesive strength. Moreover, the computational results emphasize the existence of a sharp upturn in dynamic fracture toughness in high strength structural steels at a material characteristic limiting crack tip speed even at test temperatures as low as -80°C and under ultra high crack tip loading rates ($\dot{K}_I \approx 10^8$ MPa $\sqrt{\text{m}}$/s).

* Corresponding author: Fax: 001 216 368 6445; E-mail: vxp18@po.cwru.edu

0020–7683/99/$ - see front matter
PII: S0020–7683(98)00151–6

1. Introduction

A central issue in the dynamic failure of engineering materials due to stress wave loading is the effect of material inertia and strain rate sensitivity on the initiation and propagation of fracture from a pre-existing crack tip. Significant inertial effects can arise either due to rapidly applied loading on the cracked solid and/or from rapid crack propagation (Freund, 1990). Strain rate effects have generally been regarded as making elastic–viscoplastic materials to appear more brittle. This increased propensity for brittle failure can be attributed to the elevation in the material's flow stress, due to its strain rate sensitivity, to a critical level required for initiating cleavage failure before significant plastic strains can accumulate and mitigate the effects of the otherwise sharp crack tip. At the same time, dynamic loading with sustained elevated plastic strain rates is capable of inducing significant levels of plastic strains in very short time, leading to blunting of the crack tip and hence crack growth by primarily deformation controlled mechanisms. In view of the possibility of these vastly different fracture modes/mechanisms, improved understanding of crack initiation and crack propagation at elevated crack-tip loading rates, with due considerations of the effect of inertia and strain rate sensitivity of flow stress, is important to the development of methodologies for designing more failure resistant structures.

Rather few solutions are available for the growth of transient tensile cracks in inelastic solids. Analyses of fast crack growth in structural metals have generally either assumed a steady state, e.g., Lam and Freund (1985), Freund and Hutchinson (1985), Mataga et al. (1987), Varias and Shih (1994), or have been based on an approach where a crack tip speed dependent material characterizing parameter, such as the dynamic energy release rate or the dynamic stress intensity factor is used in conjunction with a crack tip equation of motion, Freund (1990), e.g. Brickstad and Nilsson (1980), Ravichandran and Clifton (1989), Prakash and Clifton (1992). Also, in elastic–plastic analyses of rapid crack propagation a number of different crack growth criteria based on critical values of the crack-tip opening displacement, the crack-tip-opening angle, or a conservation integral (Ahmad et al., 1983; Hoff et al., 1991), have been employed. Recently, Premack and Douglas (1995), have carried out a three-dimensional FEM analysis of impact fracture of 4340 steel. The analysis makes use of the measurements of crack-tip-opening displacements and includes the effect of crack curvature, the residual plastic strain due to pre-cracking, and the strain-rate sensitivity of flow stress, to calculate the dynamic toughness of 4340 steel. In other analytical and computational approaches, a simple strip yield model has been used by Lee and Freund (1990) to gain insight in the effect of material rate-dependence on fracture mode transition. Solutions to this problem make it possible to construct curves of critical stress intensity factor vs crack-tip speed for different levels of viscosity, showing the transition between two different fracture modes. Another approach involves the use of physically based models of micromechanics of failure into the material's constitutive description (Needleman and Tvergaard, 1991; Tvergaard and Needleman, 1993), or the cell model of Broberg (1979) where brittle fracture involves the loss of stress carrying capacity over a volume (or area). In particular, Johnson (1992, 1993) has carried out finite element calculations of rapid crack growth in brittle solids using a cell damage model where the linear elastic stiffness tensor is multiplied by a factor that is a function of the relative density and that decreases from unity to zero with decreasing density.

In the present study, results of plate impact fracture experiments (Prakash, 1993) conducted on high strength 4340VAR steel at lower than room temperature, are used to provide a perspective

on dynamic fracture models incorporating the decohesion of potential fracture surfaces, with a focus on needs for improved modeling and on understanding qualitative features of dynamically propagating cracks under nominally brittle conditions. The experiments are designed to subject a pre-cracked disk to a large amplitude tensile pulse with a sharp wave-front under essentially fully plane strain loading conditions. The loading results in the onset of crack extension in less than a microsecond. The resulting crack-tip loading rates at crack initiation are of the order of $\dot{K}_I \approx 10^8$ MPa $\sqrt{\text{m}}$/s.

In order to ascertain the validity of the various dynamic fracture models, the free surface motion of the target plate are compared with the predictions of the free-surface particle velocity history obtained by employing a cohesive surface constitutive relation which allows for the creation of new free surfaces. Analytical solutions for crack-tip quantities such as the history of the stress intensity factor, under the assumptions of small scale yielding, are available for a semi-infinite crack in an infinite isotropic body under plane wave loading (Achenbach and Nuismer, 1971; Freund, 1973). However, such solutions are not available for far-field quantities such as particle velocities and stresses for cracks propagating non-uniformly under stress-wave loading conditions. Thus, in the present investigation, a numerical solution for the far field quantities of interest is sought by employing a transient finite element analysis. The finite element analyses is carried out within a framework where the continuum is characterized by two constitutive relations; one that relates stress and strain in the bulk material, and the other relates the traction and separation across a specified set of cohesive surfaces. The bulk material is characterized as an isotropically hardening and thermally softening elastic–viscoplastic von Mises solid. The fracture characteristics of the material are embedded in a cohesive surface traction–displacement separation relation, Needleman (1987). The cohesive surface framework has been used previously to address issues regarding void nucleation (Tvergaard, 1990; Povirk et al., 1991; Xu and Needleman, 1993), quasi-static crack growth in plastically deforming solids, (e.g. Needleman, 1990a, b; Tvergaard and Hutchinson, 1992, 1993), stability of the separation process (Suo et al., 1992; Levy, 1994), and dynamic crack growth in elastic solids (e.g. Xu and Needleman, 1994). Crack initiation, crack growth and crack arrest emerge naturally as outcomes of the imposed loading and are calculated directly in terms of the properties of the material and of parameters characterizing the cohesive surface separation law. The cohesive surface parameters include a strength and a work of separation per unit area, so that, from dimensional considerations a characteristic length enters the formulation. The model predictions for the target free surface particle velocity history are compared with the experimental observations to gain insight into the structure of the cohesive surface traction–displacement separation relationship for dynamically propagating cracks in high strength structural steels under nominally brittle conditions. In addition to modeling of crack advance, the near crack tip fields are examined to gain insight into the critical conditions that prevail in the vicinity of dynamically propagating cracks at ultra-high crack tip loading rates.

2. Plate impact fracture experiments

2.1. Experimental configuration

The experiment involves the plane strain loading of a plane crack by a step tensile pulse with duration of approximately 1 μs. The loading is achieved by impacting a disk–shaped specimen

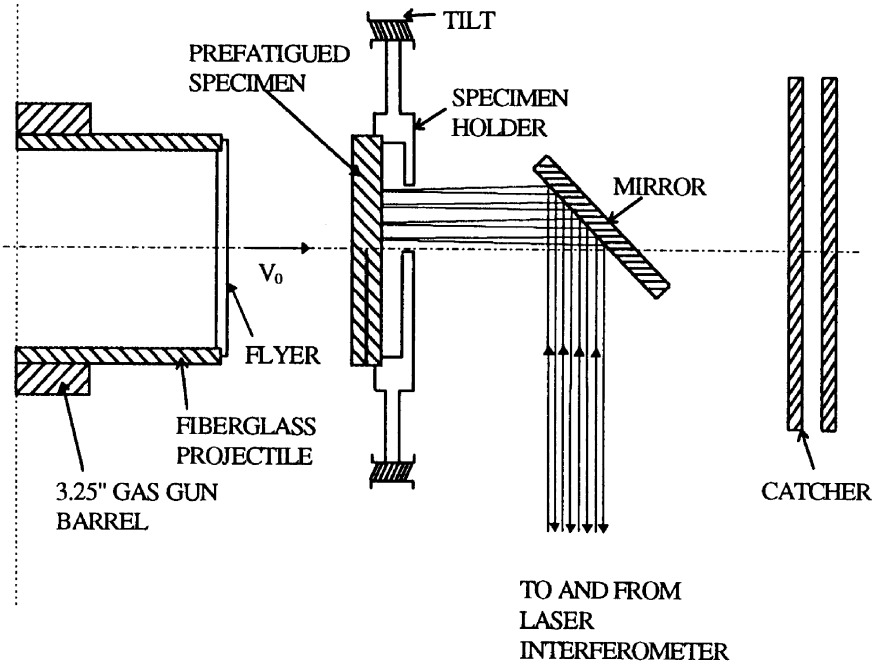

Fig. 1. Schematic of the experimental configuration.

containing a mid-plane crack by a thin flyer plate fabricated from the same material as the specimen, in a plate impact loading device as shown in Fig. 1. The specimen is machined from a notched cylindrical bar in which a fatigue crack has been grown by subjecting the bar to cyclical bending (Ravichandran, 1983). The fatigue crack is grown in accordance with ASTM specifications for plane strain fracture toughness testing (ASTM, 1965 and ASTM, 1970). Impact occurs in a vacuum chamber that has been evacuated to a pressure of 60–80 μm of Hg and is part of a single stage gas-gun assembly. Upon impact, compressive waves of uniaxial strain are generated; one that propagates in the specimen and another that propagates in the flyer. The wave propagating through the specimen reflects from the rear surface of the specimen of as a plane tensile pulse, and it is this wave which loads the crack in tension. Upon interaction with the crack plane the plane tensile pulse is diffracted to generate a cylindrically diffracted longitudinal wave, a cylindrically diffracted shear wave and head waves. Figure 2(a) shows the non-uniform scattered fields radiating out from the crack edge. The leading wave-front is a cylindrically diffracted longitudinal wave, of radius $C_L t$, centered at the crack edge. Due to the coupling of dilatational and shear waves, the scattered field includes a cylindrical shear wave-front, of radius $C_s t$, centered at the crack edge, and the associated plane fronted headwaves travelling as speed C_s. Details of experimental procedure used for specimen preparation and executing the plate impact fracture experiments are provided in Ravichandran and Clifton (1989) and Prakash and Clifton (1992).

The time–distance diagram for the wave fronts that traverse the specimen and the flyer plate is shown in Fig. 2(b). The compressive wave that propagates through the specimen reaches the rear surface of the specimen at time t_1. The compressive wave that travels in the flyer reflects from the

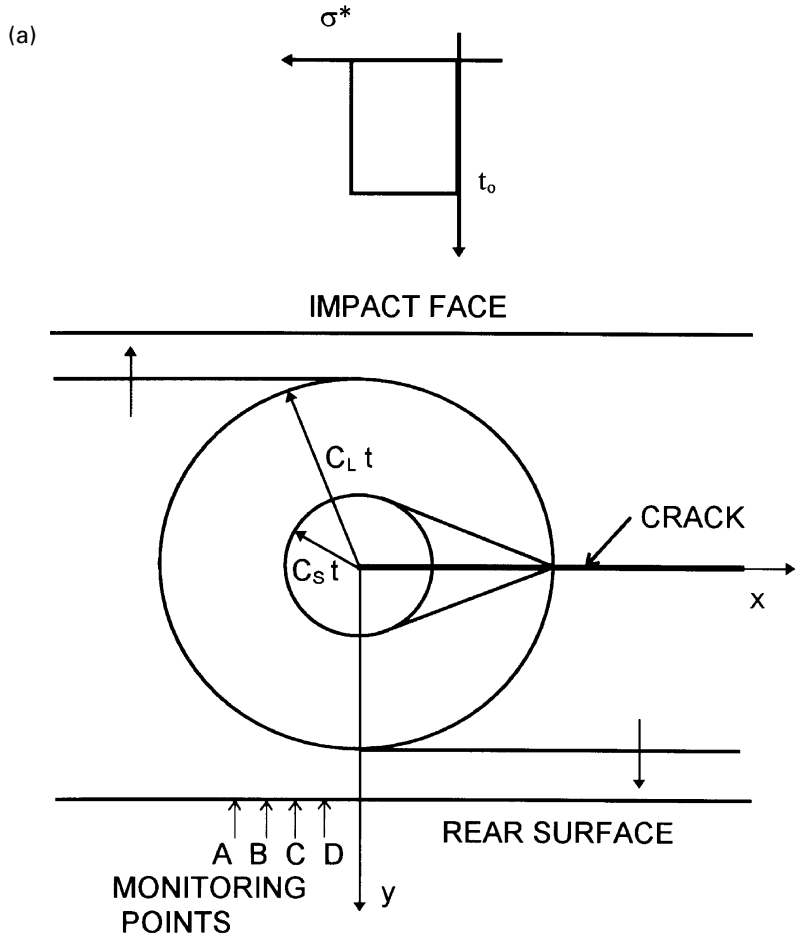

Fig. 2. (a) Wave-fronts for diffraction of a plane wave by a semi-infinite crack. (b) Wave propagation in the flyer and the specimen.

rear surface of the flyer as a plane tensile wave-front and propagates back towards the specimen. This unloading wave from the flyer removes the pressure that was imposed on the crack plane by the initial compressive pulse, leaving the crack-faces traction free. The velocity of the free surface of the specimen remains constant at the impact velocity V_0, until the unloading wave reflected from the rear surface of the flyer arrives at the rear surface of the target plate at time, t_{u1}. This unloading wave brings the rear surface velocity of the specimen to zero. During this time interval, the compressive wave reflected from the rear surface of the specimen plate arrives at the traction-free crack plane as a tensile pulse at time, t_c. The cylindrically diffracted longitudinal wave arrives at the rear surface of the specimen plate at a point directly opposite the crack tip at time, t_d. Tensile loading of the crack plane continues until the time, t_e, at which the end of the tensile pulse arrives. The corresponding diffracted longitudinal wave arrives at the rear surface of the specimen plate at time, t_f. Thus, the time interval (t_d, t_f) is the interval of primary interest in the experiment.

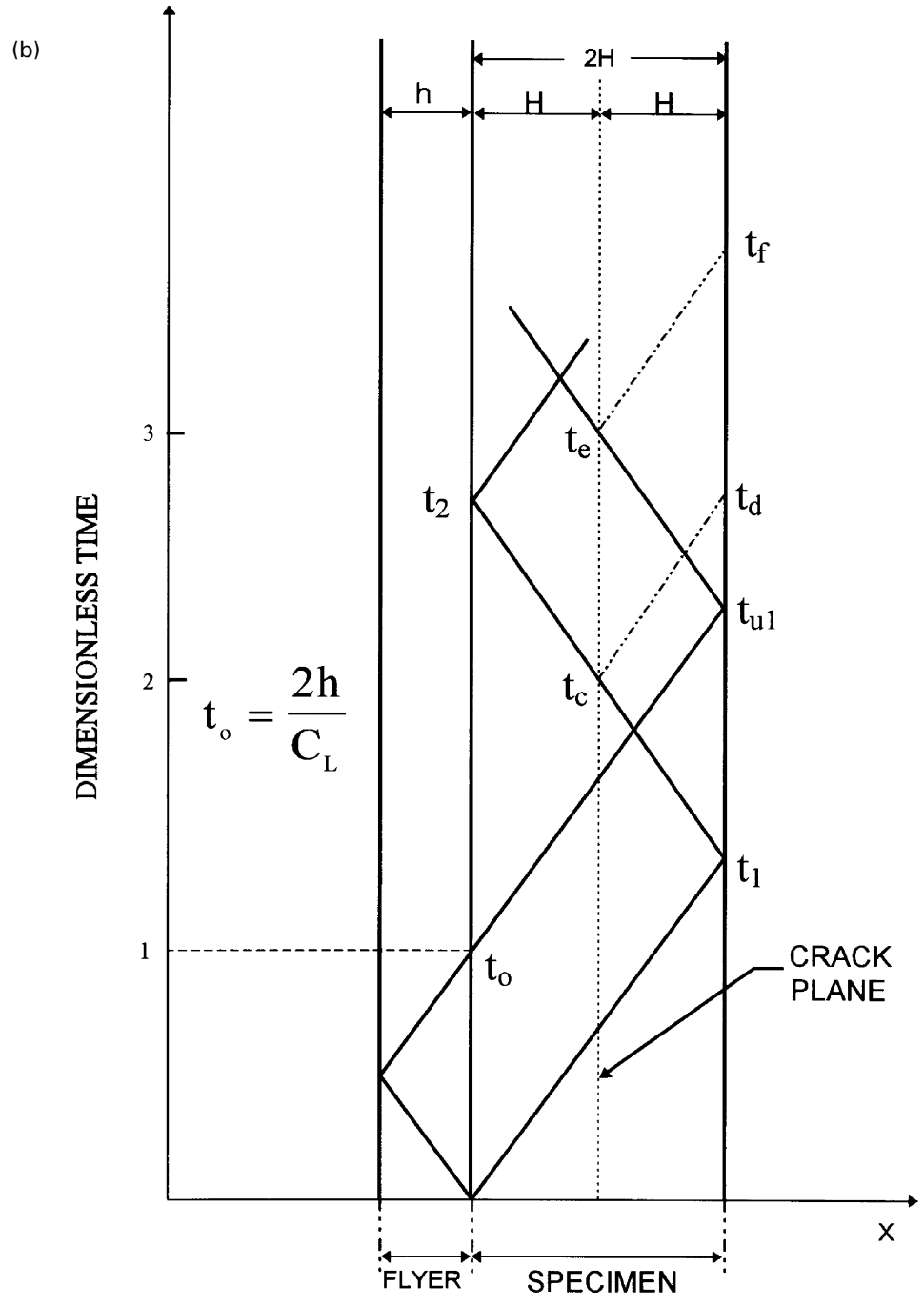

Fig. 2—continued.

A four-point normal displacement interferometer is used to measure the rear surface motion of the specimen. With this interferometer, the motion of four different points on the specimen surface can be measured simultaneously during the experiment. This is important, since unlike the conventional plate impact experiments where the rear surfaced motion is independent of in-plane coordinates, a two-dimensional field is generated by the diffraction of the plane wave by the crack. By relating the motion of the rear surface at several points on the specimen rear surface to the initiation and propagation of the crack, a better evaluation of various fracture models can be obtained. Details of the four-point laser interferometer employed in the experiments for measuring the target rear surface motion can be found in Mello et al. (1991).

In the design of the experiments, the dimensions of the specimen plate are adjusted such that the unloading waves from the lateral surface of the target plate arrives at the monitoring points after the time t_f. This condition ensures that the loading conditions for the dynamic fracture experiment are essentially exactly those of plane strain, at least until the diffracted waves from the lateral boundary reach the center of the specimen. This feature greatly facilitates the detailed correlation of theory and experiment, since for two-dimensional fracture dynamics numerical solutions can be obtained with acceptable levels of computational effort. The simplification of the loading conditions in the present experiment is obtained at the expense of lost accessibility to the crack tip measuring its velocity and the intensity or the amplitude of the local stress and deformation fields. However, as it will be shown in Section 4, the experimentally measured motion of the free surface of the specimen is quite sensitive to the critical crack tip quantities such as the critical stress intensity factor and the crack-tip speed, and the near tip quantities of interest can be readily inferred from the measurements of the free surface motion through existing analyses and finite element computations.

2.2. Theoretical background

The loading pulse has a duration $t_0 = 2h/C_L$, where h is the thickness of the flyer plate, and C_L is the speed of propagation of longitudinal waves in 4340VAR steel. The tensile stress of loading pulse, σ^*, is given by

$$\sigma^* = \tfrac{1}{2}\rho C_L V_0, \tag{1}$$

where ρ is the mass density and V_0 is the projectile velocity measured during the experiment.

For a loading of pulse of duration t_0, the transient stress intensity factor for the present model problem is given by Freund (1990) as

$$K_I(t) = n(v)\sigma^* C_L^{1/2}[t^{1/2} - (t-t_0)^{1/2}H(t-t_0)]. \tag{2}$$

In (2) $H(t)$is the Heaviside unit step function, and $n(v)$ is given by

$$n(v) = \frac{2}{(1-v)}\left(\frac{1-2v}{\pi}\right)^{1/2}, \tag{3}$$

where v is the Poisson's ratio. The crack-tip stress intensity factor, for the stationary crack increases in proportion to $\sqrt{t}$ for $0 < t < t_0$. For $t > t_0$, the stress intensity factor decreases due to the unloading term in proportion to $\sqrt{t-t_0}$. The largest value of the stress intensity factor reached is

Table 1
Chemical composition and the physical properties of the AISI 4340VAR steel employed in the present investigation

C	Mn	Ni	Cr	Mo	Cu	Si	Al	*p*	*S*	*N*	*O*	*H* ppm
0.42	0.46	1.74	0.89	0.21	0.28	0.19	0.031	0.009	0.001	0.005	0.001	1.0

(a) Heat treatment : normalize at 900°C for 2 h, austenitize at 850°C for 2 h, followed by rapid quenching in ice brine solution, temper at 200°C for 2 h, air cool.
(b) Hardness: 55–56 HRC.
(c) Mass density: $\rho = 7600$ Kg m^{-3}.
(d) Poisson's ratio: $v = 0.3$.
(e) Longitudinal wave speed: $C_L = 5.983$ mm/μs.
(f) Shear wave speed: $C_s = 3.124$ mm/μs.
(g) Rayleigh wave speed: $C_R = 2.987$ mm/μs.

$n(v)\sigma^*\sqrt{C_L t_0}$ so that the crack will initiate only if $n(v)\sigma^*\sqrt{C_L t_0} > K_{Id}$, the critical value of the dynamic stress intensity factor for the material.

Subsequently, the crack initiation time, τ, is given by

$$\tau = \frac{1}{n^2(v)C_L}\left(\frac{K_{Id}}{\sigma^*}\right)^2. \tag{4}$$

Knowing τ and using (2), the dynamic fracture toughness, K_{Id}, and the crack tip loading rate, $\dot{K}_I$, can be expressed as

$$K_{Id} = n(v)C_L^{1/2}\sigma^*\tau^{1/2} \quad \text{and} \quad \dot{K}_I = \frac{K_{Id}}{2\tau}, \tag{5}$$

respectively.

2.3. Experimental results

The material used in the present study is AISI 4340VAR steel. This material is a high strength, low ductility, structural alloy having reduced levels of phosphorus and sulfur to enhance the fracture toughness. The material is heat treated by normalizing at 900°C for 2 h, austenizing at 850°C for 2 h, and then rapidly quenching in an ice-brine solution. The heat treatment ensures a hardness of 55–56 on the Rockwell C scale. The chemical composition as well as the physical properties of the AISI 4340VAR steel employed in the present investigation are shown in Table 1.

In the present paper, the results of plate-impact fracture experiment conducted at lower than room temperature (−80°C), are discussed. The low temperature of the test ensures fracture of 4340VAR steel in a primarily brittle mode. Table 2 summarizes the experiment described in the present manuscript. It gives the impact velocity V_0, the applied normal tensile stress σ^*, and the duration of the pulse, t_0. It should be noted that the magnitude of the applied normal stress σ^*, corresponds to approximately 47% of the Hugoniot elastic limit for the 4340VAR steel employed in the present study.

Table 2
Summary of the low temperature experiment on 4340VAR steel

Impact velocity (m/s)	Stress pulse amplitude (MPa)	Pulse duration (μs)	Crack growth (mm)	Test temp. (°C)
59.0	1342.0	1.01	1.3	−80

The solid lines in Fig. 3 correspond to the experimentally recorded velocity–time profiles at the four monitoring points on the free surface of the specimen. The data shown corresponds to the time interval of primary interest, i.e. between t_d and t_f on the time–distance diagram (Fig. 2). The closest monitoring point is 0.6 mm ahead of the crack tip. The remaining three monitoring points are spaced at 0.7 mm intervals. The zero of the time scale corresponds to the first arrival of the longitudinal wave at the closest monitoring point. The curves with the lowest (Curve A) and the

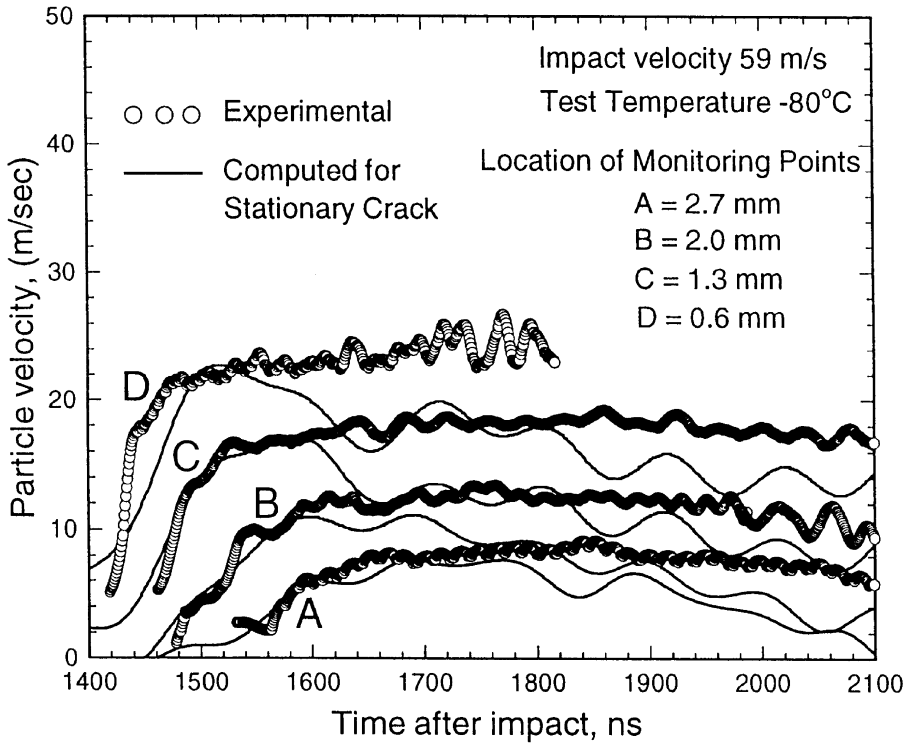

Fig. 3. Measured free-surface particle velocity history at the four monitoring points (A–D) on the free surface of the target plate, along with the computed free-surface particle velocity history for which the crack shield stationary. The time shown on the time axis is measured from the moment of impact. The crack initiation point is identified by the time at which the measured free surface particle velocity profiles separate from the computed free surface particle velocity history for the stationary crack.

highest (Curve D) velocity–time profiles correspond to the farthest (Point A) and the closest (Point D) monitoring points, respectively. The delay time between the traces correspond closely to the difference in arrival times of waves diffracted from the crack tip. The dashed curves correspond to the numerical simulation using a temperature dependent elastic–viscoplastic material model, and assuming that the crack remains stationary (details of the finite element method employed to obtain the diffracted free surface particle velocity field are provided in Section 3). Agreement between the computed and experimentally obtained velocity–time profiles is observed to be good up to approximately 115 ns after the arrival of the cylindrically diffracted waves longitudinal waves at the free surface of the target plate. Thereafter, the experimentally and computed profiles separate. This separation point is understood to be the time of crack initiation. The experimental record after the separation point corresponds to crack propagation phase of the experiment. Using the crack initiation time $\tau = 115$ ns, and eqn (5), the dynamic fracture toughness, K_{Id}, can be estimated to be 36 MPa$\sqrt{\text{m}}$. Also, the crack tip loading rate, $\dot{K}_I$, at crack initiation, can be estimated to be 1.2×10^8 MPa$\sqrt{\text{m}}$/s. It should be noted that the use of the elastodynamic solutions for the dynamic fracture toughness and the crack tip loading rates, i.e., the use of eqns (1)–(5), are valid for the analysis of the low temperature fracture experiment described here because of the existence of small scale yielding condition in the vicinity of the crack tip at crack initiation.

Figure 4(a) shows a fractograph representative of the region in the vicinity of the crack initiation site. The multifaced surface is typical of cleavage fracture in a crystalline material; each facet corresponds to a single grain. The river patterns on each facet are also typical of cleavage fracture. Presumably the cleavage facets are across grains for which the cleavage planes were favorably oriented to the crack front. Since the grains are not always favorably oriented to the fracture path for cleavage, fracture propagates in a tortuous path and is accompanied by limited plastic flow. Figure 4(b) shows a magnified view of a typical cleaved grain. The grain boundary is surrounded by small voids, suggesting that cleavage of the grains is accompanied by void growth at the grain boundaries. The grain size is typically 15 μm and voids at the grain boundary have diameters of 0.5–1.0 μm. Figure 4(c) shows a fractograph depicting the entire crack growth during the experiment. As can be observed from the fractograph, fracture occurs predominantly by cleavage and is accompanied by ductile failure processes, especially during the latter part of crack growth. Figure 4(d) shows a typical fractograph from the latter part of the crack growth region showing the presence of a void sheet.

From the aforementioned observations of the fracture surfaces, it is expected that besides the energy required for the decohesion/cleavage of the grains, a substantial fraction of the fracture energy is consumed in the inelastic processes involving initiation, growth and coalescence of voids as the brittle fracture front advances through the material. Moreover, since in the present experiment, crack initiation and crack propagation occurs within a sub-microsecond range, the growth of these voids is estimated to involve strain rates in the excess of 10^5/s. The possibility of the presence of such ultra-high plastic strain-rates during material failure in the present experiments, is of importance in the interpretation of the experimental results in view of the enhanced strain rate sensitivity of 4340VAR steel as strain rates in excess of 10^5/s. The elevation of the material's yield stress is expected to lead to an increase in energy required for sustaining inelastic deformation, especially during the latter part of crack growth. Thus, in a continuum sense, the mode of failure during crack growth can be regarded as quasi-cleavage and the analysis pertaining to the present experiment includes inelastic effects.

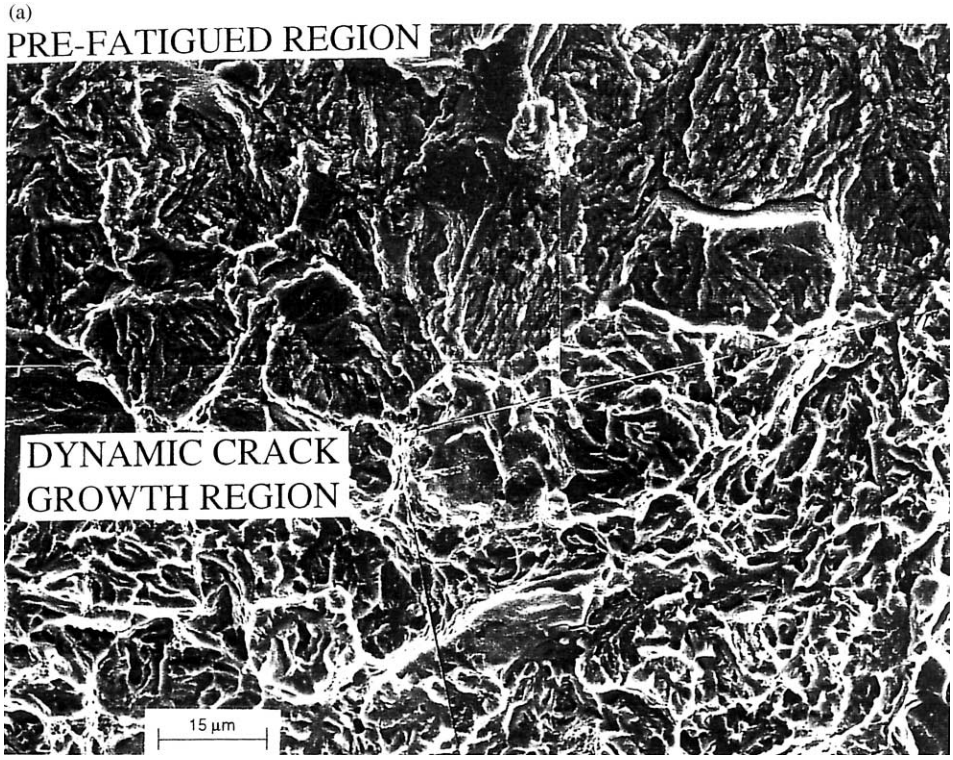

Fig. 4. (a) Fractograph of the fractured region in the vicinity of the crack initiation site showing quasi-cleavage mode of failure. (b) Fractograph showing a view of the cleaved grain along with the voids on the grain boundary. (c) Fractograph showing crack growth during the entire duration of the loading pulse. The total crack extension is estimated to be approximately 1.3 mm. (d) View of a typical void sheet formed in the fracture region corresponding to the later part of crack growth.

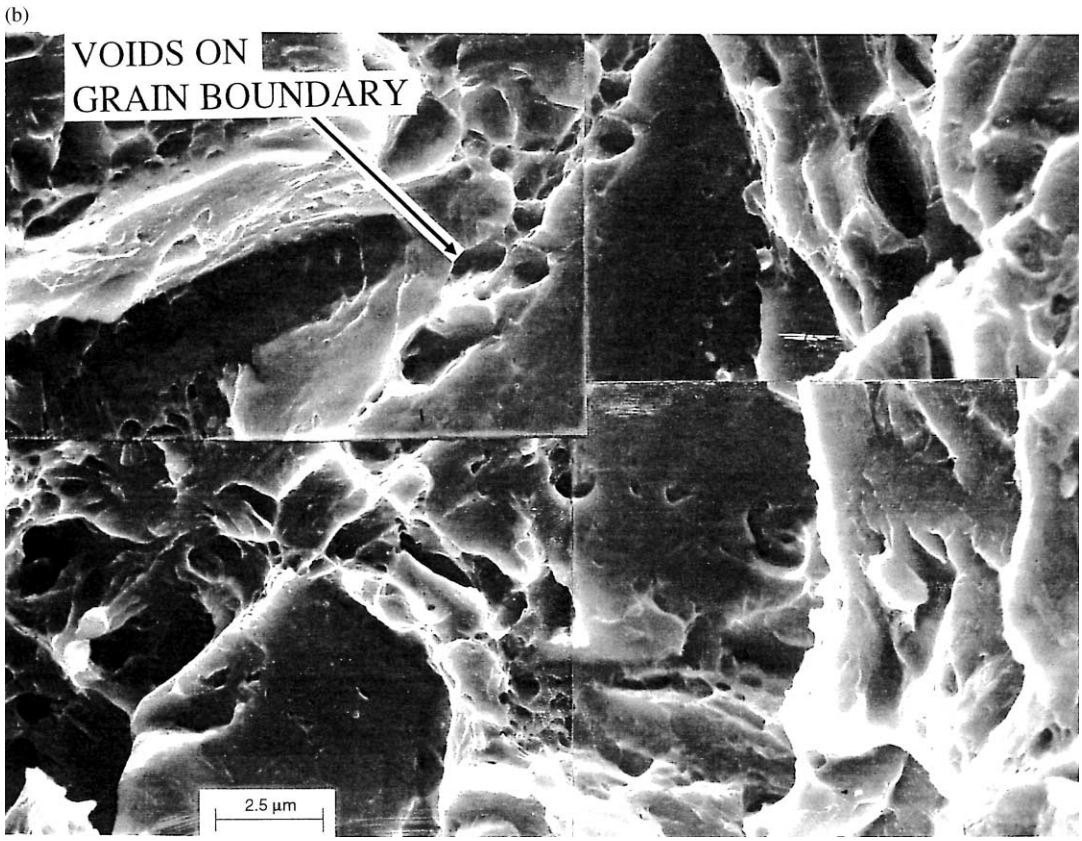

Fig. 4—continued.

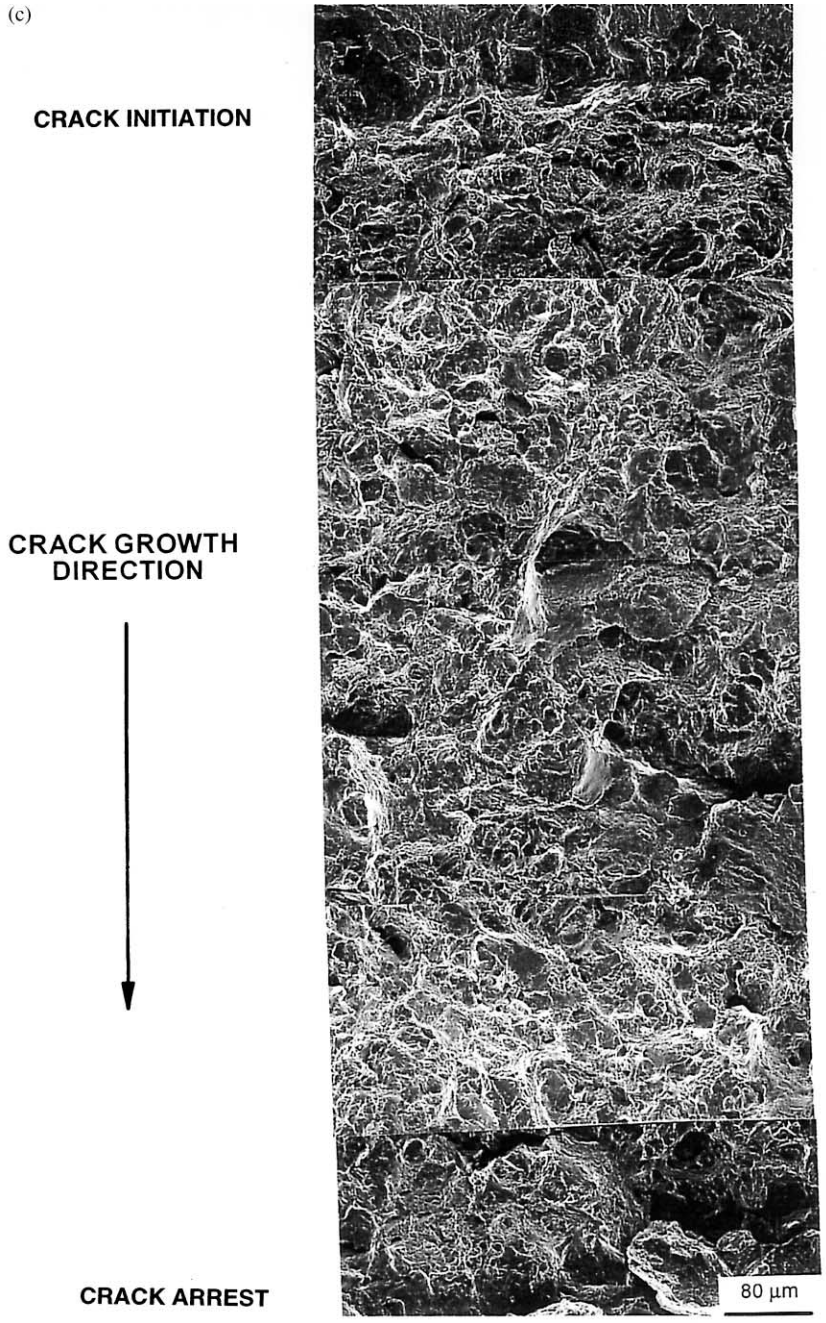

Fig. 4—continued.

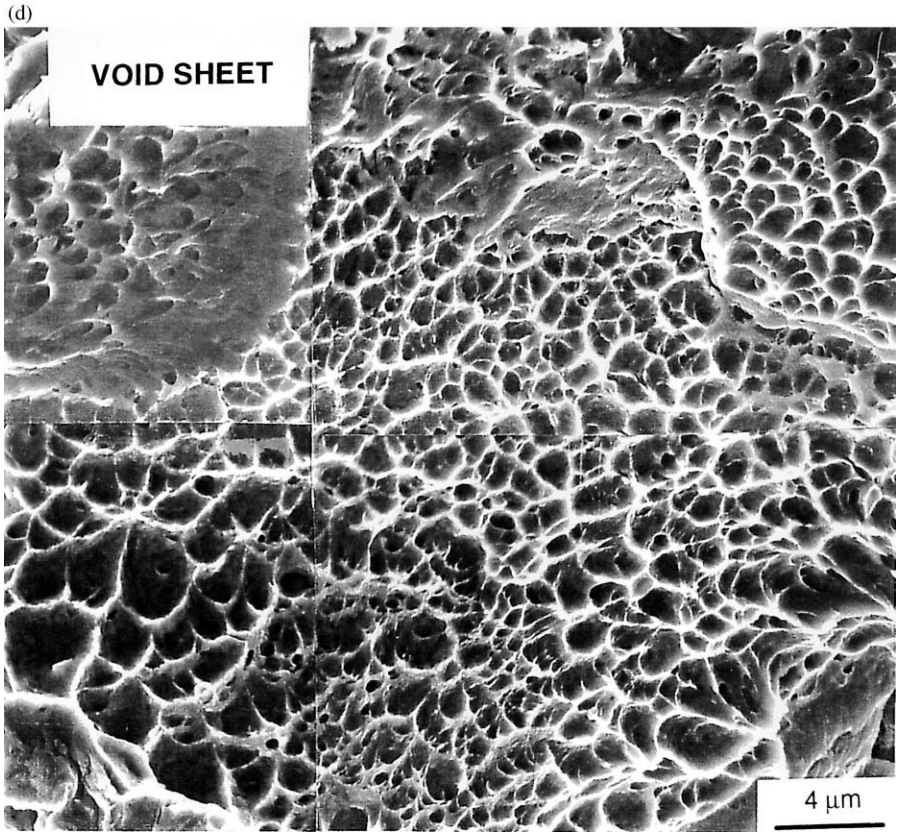

Fig. 4—continued.

3. Computational analysis

One of the objectives of the present study is to critically examine the applicability of dynamic fracture models incorporating a cohesive surface constitutive relation for sustained quasi-cleavage crack growth in high strength ferritic steels. To accomplish this objective a cohesive surface formulation, similar to the one proposed by Xu and Needleman (1994) and Seigmund and Needleman (1997), is employed. The continuum is characterized by two constitutive relations; a volumetric constitutive law of an isotropically hardening and thermally softening elastic–viscoplastic von Mises solid, and a cohesive surface constitutive relation involving the tractions and displacement jumps across the cohesive surface. The behavior that is captured is that, as the cohesive surface separates, the magnitude of the traction at first increases, reaches a maximum and then approaches zero with increasing separation. Crack initiation and crack growth emerge naturally as outcomes of the imposed loading and are calculated directly in terms of the properties of the material and of the parameters characterizing the cohesive surface separation law, which include a strength and the work of separation per unit area. Various, vastly different mechanisms give rise to this sort of response; for example, separation of atomic planes (Rose et al., 1981) and ductile void growth and coalescence (Tvergaard and Hutchinson, 1992). What distinguishes the various mechanisms is the stress required for separation, the length scale over which the separation process takes place and the dissipation accompanying the separation process.

3.1. Problem formulation

The transient finite element analysis accounts for the effects of finite geometry changes, material inertia, material rate sensitivity and heat condition. Although the elastic as well as the plastic strains in the bulk of the specimen remain small, a finite element formulation consistent with large deformation constitutive theory is employed to properly account for any large local strains and rotations accompanying the separation of the cohesive surfaces.

The analysis is based on a convected Lagrangian formulation of field equations with the initial underformed body configuration as the reference. Convected coordinates y^i are introduced which serve as particle labels. Relative to a fixed Cartesian frame, the position of a material point in the reference configuration is denoted by $\mathbf{X}(y^i)$. The corresponding material particle in the current configuration is located by a position vector $\mathbf{x}(y^i)$. The base vectors for the reference and the current configuration of the body are denoted by $\mathbf{g}_i$ and $\bar{\mathbf{g}}_i$, respectively, with

$$\mathbf{g}_i = \frac{\partial \mathbf{X}}{\partial y^i} \quad \text{and} \quad \bar{\mathbf{g}}_i = \frac{\partial \mathbf{x}}{\partial y^i}. \tag{6}$$

The displacement vector, $\mathbf{u}$, and the deformation gradient tensor, $\mathbf{F}$, are defined as

$$\mathbf{u} = \mathbf{x} - \mathbf{X} \quad \text{and} \quad \mathbf{F} = \frac{\partial \mathbf{x}}{\partial \mathbf{X}}. \tag{7}$$

The momentum balance for dynamic deformation of solids, can be written either in the current configuration in terms of the symmetric Cauchy stress tensor, $\boldsymbol{\sigma}$, or in the reference configuration in terms of the symmetric nominal stress tensor (second Piola–Kirchhoff stress), $\bar{\mathbf{T}}$. These stress measures are related to the force, $\mathbf{df}$, transmitted across a material element by

$$\mathbf{df} = \boldsymbol{\sigma}^{\mathrm{T}}\bar{\mathbf{n}}\,\mathrm{d}\bar{S} = \mathbf{F}\cdot\tilde{\mathbf{T}}^{\mathrm{T}}\mathbf{n}\,\mathrm{d}S. \tag{8}$$

Here, $\mathrm{d}\bar{S}$ and $\bar{\mathbf{n}}$ denote the area and orientation of a material element in the current configuration that had a material area $\mathrm{d}S$ and an orientation $\mathbf{n}$ in the reference configuration.

The Kirchhoff stress is defined by $\boldsymbol{\tau} = \det(\mathbf{F})\boldsymbol{\sigma}$. Using Nanson's relation in (8), yields the relationship between the stress measures, $\tilde{\mathbf{T}}$ and $\boldsymbol{\tau}$

$$\tilde{\mathbf{T}} = \mathbf{F}^{-1}\cdot\boldsymbol{\tau}\cdot\mathbf{F}^{-\mathrm{T}}. \tag{9}$$

Within the context of the finite Lagrangian formulation, the dynamic principle of virtual work can be rewritten so as to include the contribution of the cohesive surface (Xu and Needleman, 1994),

$$\int_v \tau^{ij}\delta E_{ij}\,\mathrm{d}V - \int_{S_{\mathrm{int}}} T^i\delta\Delta_i\,\mathrm{d}S = \int_{S_{\mathrm{ext}}} f^i\delta u_i\,\mathrm{d}V - \int_v \rho_0\frac{\partial^2 u^i}{\partial t^2}u_i\,\mathrm{d}V. \tag{10}$$

In (10), Δ is the displacement jump vector across the cohesive surface; ρ_0, V, S_{int} and S_{ext} are the density, volume, internal cohesive surface area and the external surface area, respectively, of the body in the reference configuration.

The traction vector component f^i, on the surface with a unit normal vector component n_j in the reference configuration is given by

$$f^i = (\tau^{ij} + \tau^{kj}u^i_{,k})n_j. \tag{11}$$

The Lagrangian strain tensor in the reference configuration is

$$E_{ij} = \tfrac{1}{2}(u_{i,j} + u_{j,i} + u^k_{,i}u_{k,j}), \tag{12}$$

where $(),_i$ represents the covariant partial differentiation in the reference frame.

Restricting attention to two dimensions (plane strain conditions), the normal and tangential components of the displacement difference across the cohesive surface can be expressed as

$$\Delta_{\mathrm{n}} = \mathbf{n}\cdot\Delta \quad \text{and} \quad \Delta_{\mathrm{t}} = \mathbf{t}\cdot\Delta, \tag{13}$$

where $\mathbf{n}$ and $\mathbf{t}$ are the normal and tangential base vectors, respectively, to the surface at a given point in the reference configuration. Neglecting any dissipation associated with the separation process, the nominal traction vector $\mathbf{T}$ (force per unit reference area), across the cohesive surface can be obtained from a cohesive surface separation potential, ϕ, as

$$\mathbf{T} = \frac{\partial\phi}{\partial\Delta}. \tag{14}$$

Since the interfacial tractions are derived from a potential which depends on the displacement difference across the interface, the form of the potential for interfacial debonding is of importance. Rose et al. (1981) suggested an exponential form for the interfacial potential based on atomistic calculations of interfacial separation. Needleman (1987) constructed a polynomial form for the interfacial potential which possesses a convenient feature that traction vanishes at a finite separation so that there is a well-defined decohesion point. The exponential form suggested by Rose et al.

(1981) and the polynomial form proposed by Needleman (1987) was later modified by Xu and Needleman (1994) to include tangential as well as a normal separation.

The cohesive surface potential employed in the present investigation has a form to that proposed by Xu and Needleman (1994)

$$\phi(\Delta_n, \Delta_t) = \phi_n + \phi_n \exp\left(-\frac{\Delta_n}{\delta_n}\right)\left\{\left[1-r+\frac{\Delta_n}{\delta_n}\right]\frac{1-q}{r-1} - \left[q+\frac{\Delta_n}{\delta_n}\left(\frac{r-q}{r-1}\right)\right]\exp\left(-\frac{\Delta_t^2}{\delta_t^2}\right)\right\}, \quad (15)$$

where ϕ_n is the work of normal separation; δ_n and δ_t are, respectively, the normal and tangential characteristic lengths; q and r are constants defined as

$$q = \frac{\phi_t}{\phi_n} \quad \text{and} \quad r = \frac{\Delta_n^*}{\delta_n}, \quad (16)$$

respectively. In (16), Δ_n^* is the value of Δ_n after complete shear separation with $T_n = 0$.

The normal work of separation, ϕ_n, and the tangential work of separation, ϕ_t, can be expressed as

$$\phi_n = \exp(1)\sigma_{max}\delta_n \quad \text{and} \quad \phi_t = \sqrt{\frac{\exp(1)}{2}}\tau_{max}\delta_t, \quad (17)$$

where σ_{max} and τ_{max} are the cohesive surface normal and tangential strengths, respectively.

The normal and the tangential components of the cohesive surface tractions are obtained for (14) and (15) as

$$T_n = \frac{\phi_n}{\delta_n}\exp\left(-\frac{\Delta_n}{\delta_n}\right)\left\{\frac{\Delta_n}{\delta_n}\exp\left(\frac{\Delta_t^2}{\delta_t^2}\right) + \frac{1-q}{r-1}\left[1-\exp\left(\frac{\Delta_t^2}{\delta_t^2}\right)\right]\left[r-\frac{\Delta_n}{\delta_n}\right]\right\}, \quad (18)$$

and

$$T_t = 2\frac{\phi_n}{\delta_t}\frac{\Delta_t}{\delta_t}\left\{q+\left(\frac{r-q}{r-1}\right)\frac{\Delta_n}{\delta_n}\right\}\exp\left(-\frac{\Delta_n}{\delta_n}\right)\exp\left(-\frac{\Delta_t^2}{\delta_t^2}\right). \quad (19)$$

Note that (18) and (19) satisfy at the constraint that $T_n = 0$ when $\Delta_n/\delta_n = 0$, and $T_t = 0$ when $\Delta_t/\delta_t = 0$. In the present work, unless stated otherwise, it is assumed that $\delta_n = \delta_t$, $q = 1$, and $r = 0$. It should be noted that by varying the constant q and r in (15), does not effect the shape of cohesive surface separation potential curve; consequently the normal traction T_n and the tangential traction T_t are weakly dependent on the values of the parameters q and r.

Figure 5 shows the normalized generalized cohesive surface potential curves ϕ/ϕ_n, is a function of the normalized normal displacement Δ_n/δ_n (with $\Delta_t = 0$). Figure 6(a) shows the normal traction T_n, across the cohesive surface as a function of Δ_n with $\Delta_t = 0$. The maximum value of $|-T_n|$ is σ_{max} and occurs when $\Delta_n/\delta_n = 1$. The negative traction discourages penetration of the two free surfaces by the strong stiffening response of the normal cohesive traction in compression. The variation of the tangential traction T_t, as a function of Δ_t (with $\Delta_n = 0$), is shown in Figure 6(b). The location of the maximum normalized tangential traction $|-T_t/\tau_{max}|$, occurs when $|\Delta_t| = \delta_t/\sqrt{2}$.

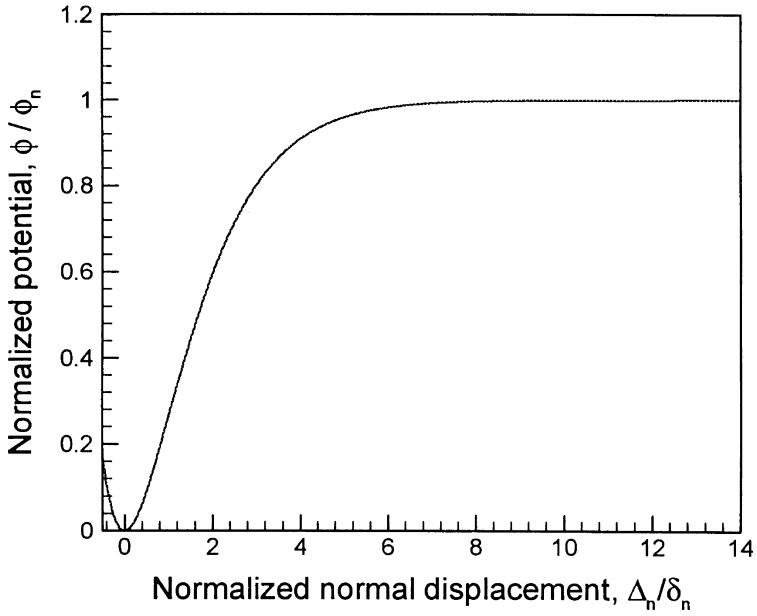

Fig. 5. Normalized cohesive surface potential as a function of the normalized normal separation Δ_n/δ_n, with $\Delta_t = 0$.

With body forces and external heat energy source being absent, the balance of energy can be expressed as integrals over the reference configuration

$$\int_v \rho_0 \dot{e}\, \mathrm{d}V + \frac{\mathrm{d}}{\mathrm{d}t}\int_v \frac{1}{2}\rho_0 \dot{\mathbf{u}}\cdot\dot{\mathbf{u}}\, \mathrm{d}V = \int_s \mathbf{f}\cdot\dot{\mathbf{u}}\, \mathrm{d}S - \int_s J\mathbf{F}^{-\mathrm{T}}\mathbf{n}\cdot\bar{\mathbf{q}}\, \mathrm{d}S, \tag{20}$$

where e is the specific internal energy, $\mathrm{d}/\mathrm{d}t$ is the material time derivative, J is the Jacobian of the deformation, and $\bar{\mathbf{q}}$ is the heat-flux vector normal to the surface in the current configuration.

The formulation of the energy balance and the equation of the heat conduction follows Povrik et al. (1990) except for the inclusion of the kinetic energy term. Assuming that the heat capacity at constant stress can be approximated by the specific heat at constant pressure c_p, and assuming small elastic strains ($J = \det|\mathbf{F}| \approx 1$, and hence $\boldsymbol{\tau} = \boldsymbol{\sigma}$), the balance of energy can be expressed in terms of integrals over the reference configuration as

$$\int_v \rho_0 c_p \dot{\theta}\, \mathrm{d}V = \int_v \chi\boldsymbol{\tau} : \mathbf{D}^p\, \mathrm{d}V + \int_v Jk\nabla_0\cdot(\mathbf{F}^{-1}\cdot\mathbf{F}^{-\mathrm{T}}\cdot\nabla_0\theta)\, \mathrm{d}V. \tag{21}$$

In (21) the gradient operator in the reference configuration is denoted by $\nabla_0 = \mathbf{g}^K(\partial/\partial y^K)$, and χ represents the fraction of plastic work rate converted to heat; χ is taken to have the value of 0.9, which is typical for metals (Taylor and Quinney, 1934).

Assuming the existence of a strain energy density function for elastic response, the Jaumann rate of Kirchhoff stress, $\overset{\nabla}{\boldsymbol{\tau}}$, based on the elastic spin rate $\mathbf{W}^e$, can be written as (Needleman, 1985)

$$\overset{\nabla}{\boldsymbol{\tau}} = \dot{\boldsymbol{\tau}} - \mathbf{W}^e\cdot\boldsymbol{\tau} + \boldsymbol{\tau}\cdot\mathbf{W}^e = \mathbf{L}^e : (\mathbf{D}^e - \alpha\dot{\theta}) + \boldsymbol{\tau}\cdot\mathbf{D}^e + \mathbf{D}^e\cdot\boldsymbol{\tau}, \tag{22}$$

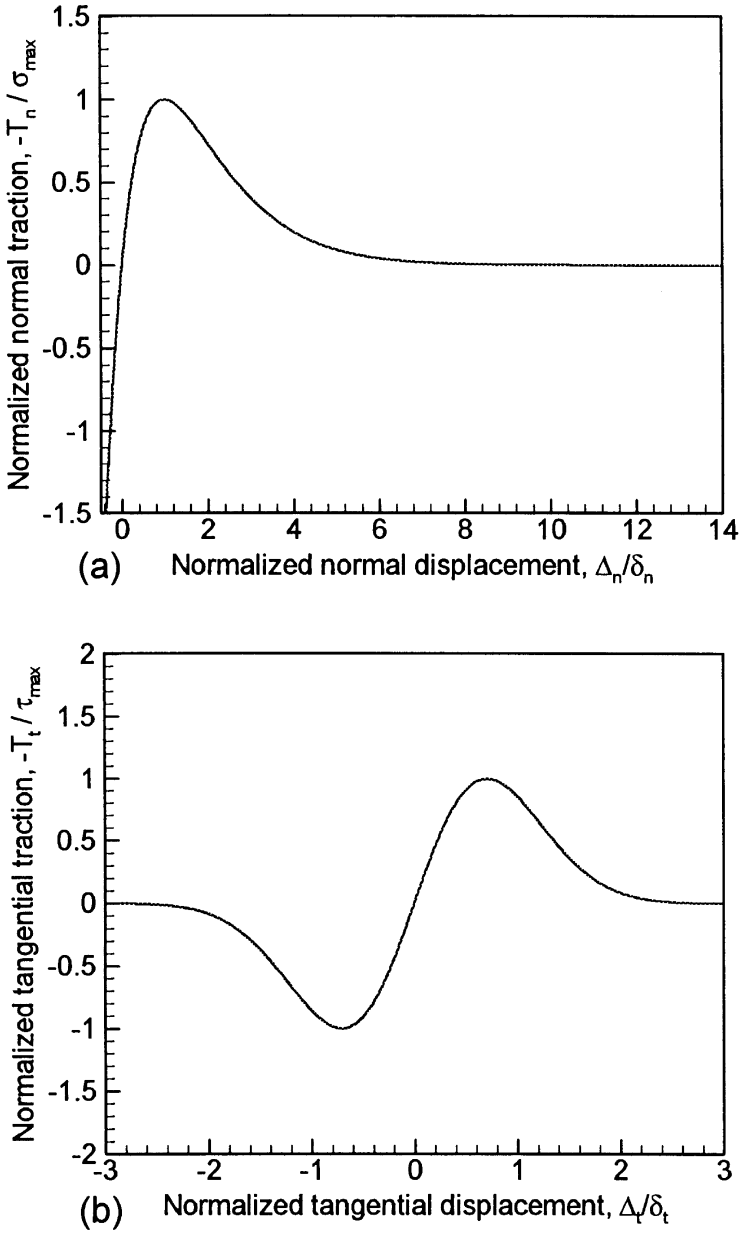

Fig. 6. (a) Normalized normal traction across the cohesive interface as a function of the normalized normal separation Δ_n/δ_n, with $\Delta_t = 0$. (b) Normalized tangential traction across the cohesive interface as a function of the normalized tangential separation Δ_t/δ_t, with $\Delta_n = 0$.

where $\overset{\nabla}{\boldsymbol{\tau}}$ is the non-objective material time derivative of the Kirchhoff stress and L^e is the elastic moduli convected with the elastic deformation gradient, i.e. $L^e = \mathbf{F}^e \cdot \mathbf{F}^e \cdot L \cdot \mathbf{F}^{eT} \cdot \mathbf{F}^{eT}$. The relation (22) is valid for finite as well as infinitesimal elastic deformations.

In applications to metal plasticity, the elastic strains generally remain small as compared to the plastic strains. This implies that the stress magnitude is small compared to the magnitude of any elastic moduli and the last two terms on the RHS of (22) are negligible in comparison with the first term. Moreover, in view of the lack of well-accepted models for the plastic spin for polycrystalline metals, $\mathbf{W}^{\mathrm{p}}$ is taken to be zero for the analysis used here. For plasticity theories with $\mathbf{W}^{\mathrm{p}}=0$ the elastic spin rate is identical to the total spin rate. Thus, the Jaumann rate of Kirchhoff stress based on the elastic spin rate can be replaced by the Jaumann rate based on the total material spin $\mathbf{W}$. The rate of deformation can be expressed as the sum of an elastic part, a thermal part and a part due to plastic straining. Hence, $\mathbf{D}=\mathbf{D}^{\mathrm{e}}+\mathbf{D}^{\mathrm{p}}+\mathbf{D}^{\mathrm{T}}$. Then, in (22), $\mathbf{D}^{\mathrm{e}}$ can be replaced by $\mathbf{D}-\mathbf{D}^{\mathrm{p}}-\mathbf{D}^{\mathrm{T}}$ and $\mathbf{W}^{\mathrm{e}}$ by $\mathbf{W}$ (since $\mathbf{W}^{\mathrm{p}}=0$), which together with $\mathbf{D}^{\mathrm{T}}=\alpha\dot{\theta}\mathbf{I}$ yields

$$\overset{\nabla}{\boldsymbol{\tau}}=\dot{\boldsymbol{\tau}}-\mathbf{W}\cdot\boldsymbol{\tau}+\boldsymbol{\tau}\cdot\mathbf{W}=\mathbf{L}^{\mathrm{e}}:(\mathbf{D}-\mathbf{D}^{\mathrm{p}}-\alpha\mathbf{I}\dot{\theta}). \tag{23}$$

When the temperature dependence of the elastic moduli is ignored, the tangent moduli for the isotropic elastic response can be written as

$$(L^{\mathrm{e}})^{ijkl}=\frac{E}{1+v}\left[\frac{1}{2}(\bar{g}^{ik}\bar{g}^{jl}+\bar{g}^{jk}\bar{g}^{il})+\frac{v}{1-2v}\bar{g}^{ik}\bar{g}^{jl}\right], \tag{24}$$

where, E is Young's modulus and v is Poisson's ratio.

For updating the Kirchhoff stresses we need the convected time-derivative of Kirchhoff stresses on the current base vectors. Using an analysis paralleling (Needleman, 1985), the convected derivative of the contravariant components of the Kirchhoff stress can be expressed as

$$\dot{\boldsymbol{\tau}}^{\mathrm{c}}=\mathbf{C}:\mathbf{D}-\mathbf{P}, \tag{25}$$

where $\mathbf{C}$ is a tensor of rank four and $\mathbf{P}=\mathbf{L}^{\mathrm{e}}:(\mathbf{D}^{\mathrm{p}}+\alpha\mathbf{I}\dot{\theta})$. On the current base vectors (23) can be written as

$$(\dot{\tau}^{\mathrm{c}})^{ij}=C^{ijkl}\dot{\mathbf{E}}_{kl}-P^{ij}. \tag{26}$$

The Lagrangian strain-rate appears in (26) via the identity $\dot{E}_{ij}=\mathbf{g}_i\cdot\mathbf{D}\mathbf{g}_j$, and its components on the reference base vectors are given by

$$\dot{E}_{ij}=\tfrac{1}{2}(F^k_i\dot{F}_{kj}+\dot{F}^k_jF_{kj}). \tag{27}$$

The components of the four tensor $\mathbf{C}$, on the current base vectors can be expressed as

$$C^{ijkl}=(L^{\mathrm{e}})^{ijkl}-\tfrac{1}{2}[\bar{g}^{ij}\tau^{jl}+\bar{g}^{jk}\tau^{il}+\bar{g}^{il}\tau^{ik}+\bar{g}^{jl}\tau^{ik}]. \tag{28}$$

The material is characterized as an isotropically hardening viscoplastic solid for which $\mathbf{D}^{\mathrm{p}}$ can be expressed using the J_2 flow theory as

$$\mathbf{D}^{\mathrm{p}}=\dot{\bar{\varepsilon}}\mathbf{p}\quad\text{where }\mathbf{p}=\frac{3\tau'}{2\bar{\sigma}}. \tag{29}$$

If (29) $\dot{\bar{\varepsilon}}$ is the equivalent plastic strain rate function; the deviatoric stress $\boldsymbol{\tau}'$ and the equivalent flow stress $\bar{\sigma}$ are given by

$$\boldsymbol{\tau}'=\boldsymbol{\tau}-\tfrac{1}{3}(\boldsymbol{\tau}:\mathbf{I})\mathbf{I}\quad\text{and}\quad\bar{\sigma}^2=\tfrac{3}{2}\boldsymbol{\tau}':\boldsymbol{\tau}'. \tag{30}$$

The material properties used in the present simulations are representative of hardened AISI 4340VAR steel. A combined power-law and exponential plastic strain-rate relation (Clifton, 1990), that gives rise to enhanced strain-rate hardening at ultra-high strain rates, e.g. Campbell and Ferguson (1970), and Klopp et al. (1985), is employed. The plastic strain rate $\dot{\bar{\varepsilon}}$, is taken to be of the form

$$\dot{\bar{\varepsilon}} = \frac{\dot{\varepsilon}_1 \dot{\varepsilon}_2}{\dot{\varepsilon}_1 + \dot{\varepsilon}_2}, \tag{31}$$

where

$$\dot{\varepsilon}_1 = \dot{\varepsilon}_0 \left[\frac{\bar{\sigma}}{g(\bar{\varepsilon}, \theta)}\right]^m, \quad \dot{\varepsilon}_2 = \dot{\varepsilon}_m \exp\left[-\frac{a g(\bar{\varepsilon}, \theta)}{\bar{\sigma}}\right] \tag{32}$$

and

$$g(\bar{\varepsilon}, \theta) = \sigma_0 (1 + \bar{\varepsilon}/\varepsilon_0)^N \{1 - \beta[(\theta/\theta_0)^k - 1]\}. \tag{33}$$

In (33)–(34), $\bar{\varepsilon} = \int_0^t \dot{\bar{\varepsilon}}\, dt$ is the equivalent plastic strain; $\dot{\varepsilon}_m$ is a reference strain rate; m and a are the material strain rate sensitivity parameters; σ_0 is a reference stress; ε_0 is the reference strain; N is the material strain hardening exponent; θ_0 is a reference temperature; and β and k are the thermal softening parameters. The function $g(\bar{\varepsilon}, \theta)$ represents the stress–strain relation at a quasi-static strain rate of $\dot{\varepsilon}_0$ and at temperature θ.

Equation (31) provides a smooth transition between the measured response $\dot{\bar{\varepsilon}} = \dot{\bar{\varepsilon}}_1(\bar{\sigma}, \bar{\varepsilon}, \theta)$ at strain rates less than $10^3\ s^{-1}$, and the limiting behavior $\dot{\bar{\varepsilon}} = \dot{\bar{\varepsilon}}_2\ (\bar{\sigma}, \bar{\varepsilon}, \theta)$ at strain rates greater than, say, $10^5\ s^{-1}$. The model includes a limiting strain rate $\dot{\varepsilon}_m$ which is not obtainable from experiments; a value of $5 \times 10^8\ s^{-1}$ or greater is chosen, primarily for avoiding the need for unreasonably small steps at early times when the shear stresses are large. These stresses are relaxed in a few nanoseconds. The uncertainty in the response of the material at small strains and at large strain rates is unavoidable at present because of the lack of experimental data in this regime.

The material response of 4340VAR steel is shown in Fig. 7. The material parameters used in the model are listed in Table 3.

Table 3
Material parameters used to describe the present model for AISI 4340VAR steel (200°C temper, $R_c = 55$)

$E = 202$ GPa
$\sigma_0 = 1895$ MPa
$c_p = 465$ J/(Kg K)
$\alpha = 1.0 \times 10^5$ 1/K
$a = 10$
$\dot{\varepsilon}_0 = 0.0094$
$k = 100$ W/m K
$T_0 = 293$ K
$\kappa = 1.0$
$N = 0.1$
$\nu = 0.3$

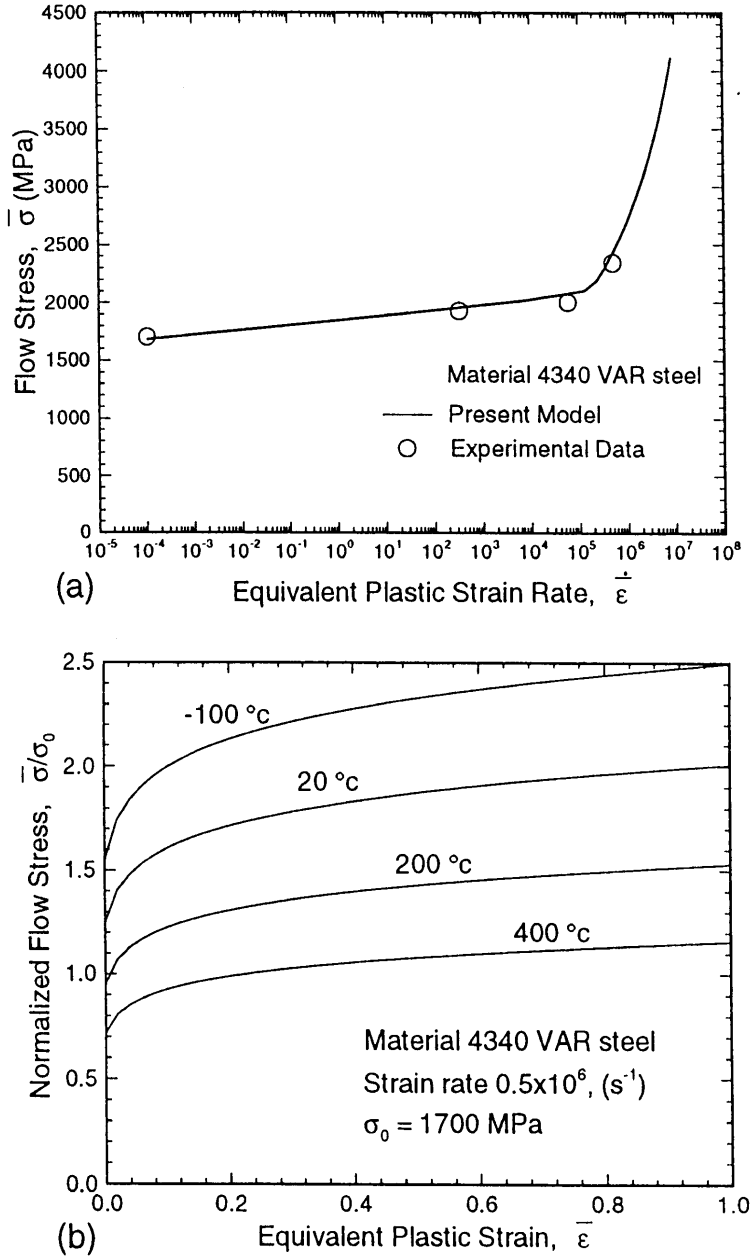

Fig. 7. Elastic–viscoplastic response of 4340VAR ($R_c = 55$) steel. (a) Enhanced plastic strain rate sensitivity of flow stress for $\dot{\bar{\varepsilon}}^p > 10^5$/s. (b) Temperature dependence of the flow stress as a function of the equivalent plastic strain at a fixed plastic strain rate.

3.2. Finite element implementation

As discussed by Budiansky (1969), the principle of virtual work (10) can be used as the variational principle for a solid continuum undergoing arbitrarily large displacements and deformations. Moreover, the variational equation governing the thermo-mechanical energy balance can be obtained form the balance of energy, (21), as

$$\int_v \rho_0 c_p \dot{\theta}\delta\theta \, dV = \int_v \chi\boldsymbol{\tau} : \mathbf{D}^p \delta\theta \, dV - \int_v Jk(\mathbf{F}^{-1}\cdot\mathbf{F}^{-T}\cdot\nabla_0\theta)\cdot\nabla_0\delta\theta \, dV + \int_s Jk\mathbf{N}\cdot\{\mathbf{F}^{-1}\cdot\mathbf{F}^{-T}\cdot\nabla_0\theta)\}\delta\theta \, dS. \quad (34)$$

When the finite-element approximations for the displacement and temperature fields are substituted into (10) and (34), the resulting equations take the form

$$\mathbf{M}\frac{\partial^2\mathbf{U}}{\partial t^2} = \mathbf{R}, \quad (35)$$

$$\mathbf{C}\frac{\partial T}{\partial t} = -\mathbf{K}\boldsymbol{\theta} + \mathbf{H}, \quad (36)$$

where $\mathbf{U}$ is the vector of nodal displacements, $\boldsymbol{\theta}$ is the vector of nodal temperatures, $\mathbf{M}$, $\mathbf{C}$, $\mathbf{K}$, are, respectively, the mass, heat capacitance, and heat conductance matrices, and $\mathbf{R}$ and $\mathbf{H}$ are the mechanical and thermal force vectors.

A lumped mass matrix is used in (35) instead of the consistent mass matrix; the lumped mass matrix has been found preferable for explicit time integration procedures for the point of veiw of computational efficiency and accuracy (Krieg and Key, 1973). An explicit time integration scheme based on the Newmark β-method, with $\beta = 0$, and $\gamma = 0.5$ (Belytschko et al., 1976) is used to integrate the equations of motion to obtain the nodal velocities and nodal displacements via

$$\frac{\partial^2\mathbf{U}^{n+1}}{\partial t^2} = \mathbf{M}^{-1}\mathbf{R}^{n+1}, \quad (37)$$

$$\frac{\partial\mathbf{U}^{n+1}}{\partial t} = \frac{\partial\mathbf{U}^{n}}{\partial t} + \frac{1}{2}\Delta t_n\left(\frac{\partial^2\mathbf{U}^{n}}{\partial t^2} + \frac{\partial^2\mathbf{U}^{n+1}}{\partial t^2}\right), \quad (38)$$

$$\mathbf{U}^{n+1} = \mathbf{U}^{n} + \Delta t_n\frac{\partial\mathbf{U}^{n}}{\partial t} + \frac{1}{2}(\Delta t_n)^2\frac{\partial^2\mathbf{U}^{n}}{\partial t^2}, \quad (39)$$

where $(\,)^{-1}$ denotes the matrix inverse.

In the applications of interest here, the mechanical equations always set the critical time for stability. It therefore suffices to lump the capacitance matrix with the result

$$\frac{\partial \theta^{n+1}}{\partial t} = \mathbf{C}^{-1}(-\mathbf{K}^n\boldsymbol{\theta}^n + \mathbf{H}^n), \tag{40}$$

and

$$\theta^{n+1} = \theta^n + \Delta t_{\mathrm{n}} \frac{\partial \theta^{n+1}}{\partial t}. \tag{41}$$

A staggered procedure (Park and Fellipa, 1983) is adopted for the purpose of coupling the thermal and mechanical equations. Mechanical and thermal computations are staggered assuming constant temperature during the mechanical step and constant heat generation during the thermal step. Following Lemonds and Needleman (1986), a mechanical step is taken first based on the current distribution of nodal temperatures. The plastic dissipation rate $\boldsymbol{\tau} : \mathbf{D}^{\mathrm{p}}$, and its contribution to the thermal force vector $\mathbf{H}^n$, is determined. Next, the thermal force vector is used in the thermal analysis where the nodal temperatures at $\mathbf{t}_{n+1}$ are recomputed by recourse to the forward Euler algorithm (40) and (41). The resulting nodal temperatures are then used in the mechanical step and incorporated into the thermal-softening model described in (31)–(33). The rate tangent modulus expansion algorithm (Pierce et al., 1984) is used to update the contravariant components of the convected Kirchhoff stress tensor, i.e., $\boldsymbol{\tau}^{n+1} = \boldsymbol{\tau}^n + \dot{\boldsymbol{\tau}}^{\mathrm{c}} \Delta t_{\mathrm{n}}$.

The computations are carried out for an edge cracked specimen shown in Figure 8(a). In veiw of the plane strain conditions prevailing in the specimen and the use of the convected Lagrangian formulation with the Cartesian coordinate system as the reference, the y^1–y^2 plane is taken to be the plane of deformation. The specimen dimensions are taken to be $w_1 = w_2 = 20.0$ mm and $b_1 = b_2 = 4.0$ mm. These dimensions ensure that no unloading waves for the lateral boundary of the specimen reach the crack tip or the monitoring points during the time duration of interest. With origin of the coordinate system at the initial crack tip, the boundary conditions can be written as

$$\begin{aligned}
&f^1 = 0, \quad f^2 = 0 \quad \text{on } y^1 = -w_1 \quad \text{(left traction–free lateral boundary)},\\
&f^1 = 0, \quad f^2 = 0 \quad \text{on } y^1 = w_2 \quad \text{(right traction–free lateral boundary)},\\
&f^1 = 0, \quad f^2 = 0 \quad \text{on } y^2 = 0 \quad \text{and} \quad y^1 < 0 \quad \text{(traction–free crack plane)}.
\end{aligned} \tag{42}$$

Moreover, to save computational time, the impact face of the specimen is taken to be traction free and initial conditions corresponding to a plane tensile pulse propagating towards the crack plane from the rear surface of the specimen, are prescribed:

$$\begin{aligned}
&f^1 = 0, \quad f^2 = 0 \quad \text{on } y^2 = -b_2 \quad \text{(impact face of the specimen)},\\
&u_2 = \int_0^1 V(t)\,\mathrm{d} \quad f^1 = 0 \quad \text{on } y^2 = b_1 \quad \text{(rear surface of the specimen)}.
\end{aligned} \tag{43}$$

The function $V(t)$ in eqn (43) is taken to be

$$V(t) = \begin{cases} V_0 t/t_{\mathrm{rise}}, & \text{for } t \leqslant t_{\mathrm{rise}},\\ V_0, & \text{for } t_{\mathrm{rise}} < t \leqslant t_{\mathrm{fall}}. \end{cases} \tag{44}$$

In (44) t_{rise} and t_{fall} are the rise time and the fall time of the loading pulse, respectively, and are taken to be $t_{rise} = t_{fall} = 75$ ns, in the present computations.

The finite element discretization is based on linear displacement triangular elements that are arranged in a 'crossed-triangle' quadrilateral pattern. In these constant strain triangular sub-elements the displacements and temperature are taken to vary linearly over the triangular elements. Nagtegaal et al. (1974) have shown that an element of this type can accommodate isochoric deformations. This is of significance since plastic strain is volume preserving, so that the total deformation at large strains is nearly isochoric.

The full finite element mesh used for the computations is shown in Fig. 8(b). In front of crack tip, a uniform mesh also referred to as the process zone, consists of 50 quadrilaterals in the y^1 direction and 10 quadrilaterals placed symmetrically about the y^2 direction. Each quadrilateral elements in the process zone has a dimension 16×10 μm. The entire finite-element mesh consists of 3980 quadrilateral elements with 19,882 degrees of freedom. Attention is focused to a single cohesive surface, which restricts crack growth along the initial crack-plane. The integration scheme to compute the integral over the internal cohesive boundary uses four Gauss points within each linear segment and the interfacial tractions are evaluated at the Gauss integration points rather at the finite element nodes. This permits partial debonding within a linear segment (Needleman, 1987). In presenting computational results, the quadrilateral is regarded as the basic element, and when reporting values of field quantities the average value of the four triangles is associated with the centroid of the quadrilateral.

4. Results and discussion

4.1. Predictions of the rate independent cohesive surface model and comparison with the experimental results

In order to make use of the cohesive surface potential in the finite element analysis, we need to estimate the parameters which control the normal and tangential cohesive surface tractions. The parameters which need to be specified are σ_{max} and δ_n (where $\delta_t = \delta_n$). Noting that for Mode I crack-like behavior in plane strain $J_{IC} = \phi_n$ (Rice, 1968), and using the relation $K_{IC} = \sqrt{EJ_{IC}/(1-v^2)}$, the cohesive surface parameters can be chosen such that the resulting ϕ_n is consistent with the low temperature dynamic fracture toughness of 4340VAR steel. Two sets of cohesive surface parameters, each consistent with $K_{IC} = 36\,\text{MPa}\sqrt{\text{m}}$, can be represented by $\sigma_{max} = E/65$ MPa and $\delta_n = \delta_t = 0.75\,\mu$m, and $\sigma_{max} = \text{E}/15$ Mpa and $\delta_n = \delta_t = 0.17\,\mu$m. Note that the first set of the cohesive surface parameters correspond to the case in which failure occurs in a predominantly inelastic manner with material separation occurring over a characteristic length 0.75 μm, whereas the second set of cohesive surface parameters correspond to a more cleavage type of failure with fracture occurring over a relatively smaller characteristic length. The experimental and the computed free surface particle velocity vs time profiles, corresponding to the two data sets, are represented in Figs 9(a)–(d) by the dashed and the dashed–dot–dot lines, respectively. From Figs 9(a)–(d) it can be seen that the predictions of the free surface particle velocity history, corresponding to the two data sets, deviate significantly from the experimental profiles. Corresponding to the first data set, the computed free surface particle velocity history results in an

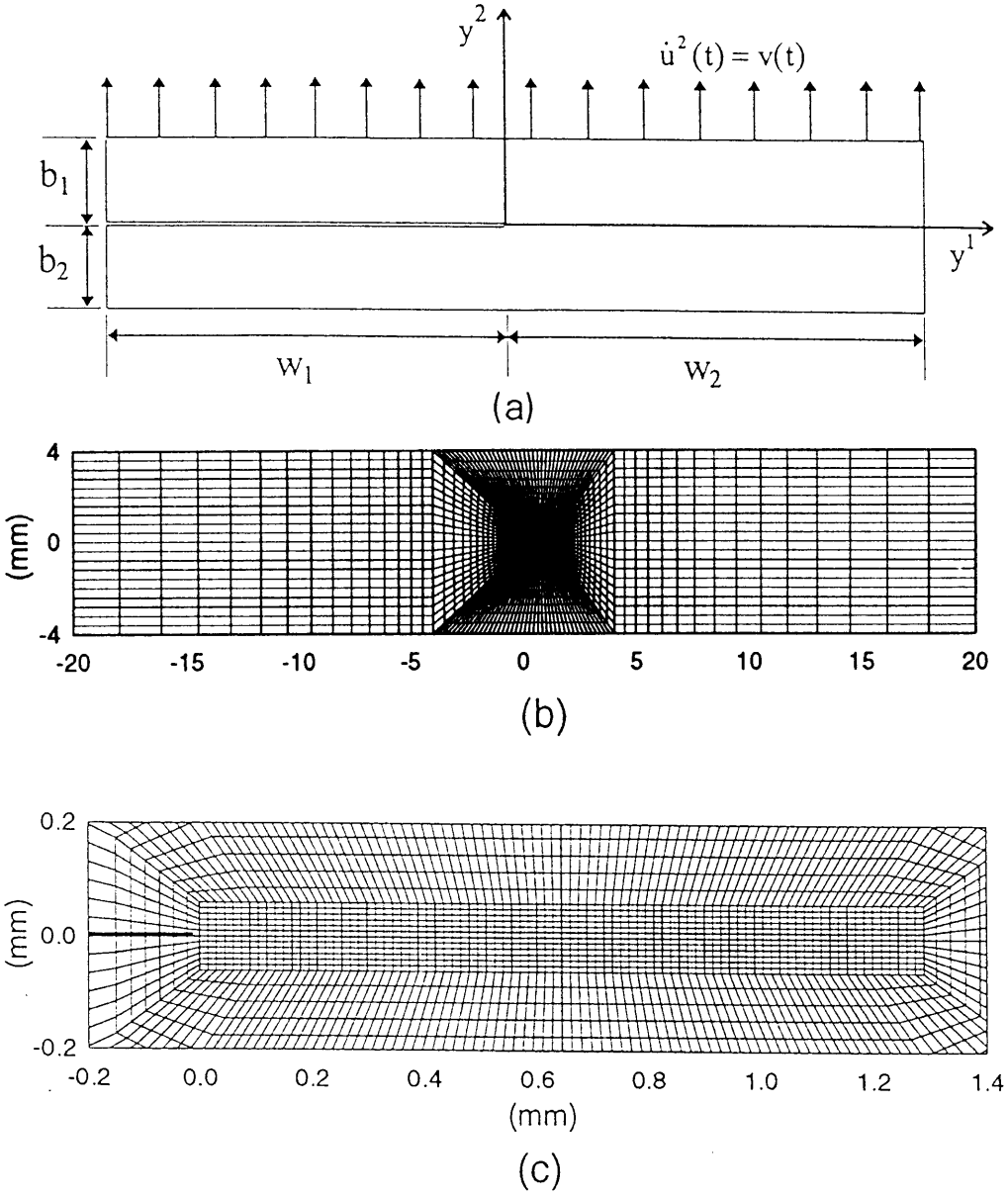

Fig. 8. (a) Geometry of the edge cracked specimen used in the finite element modeling. (b) Discretization of the geometry of the specimen using quadrilateral elements consisting of four 'crossed' triangles. (c) Discretization of the region in the vicinity of the initial crack tip, also referred to as the process zone in the text.

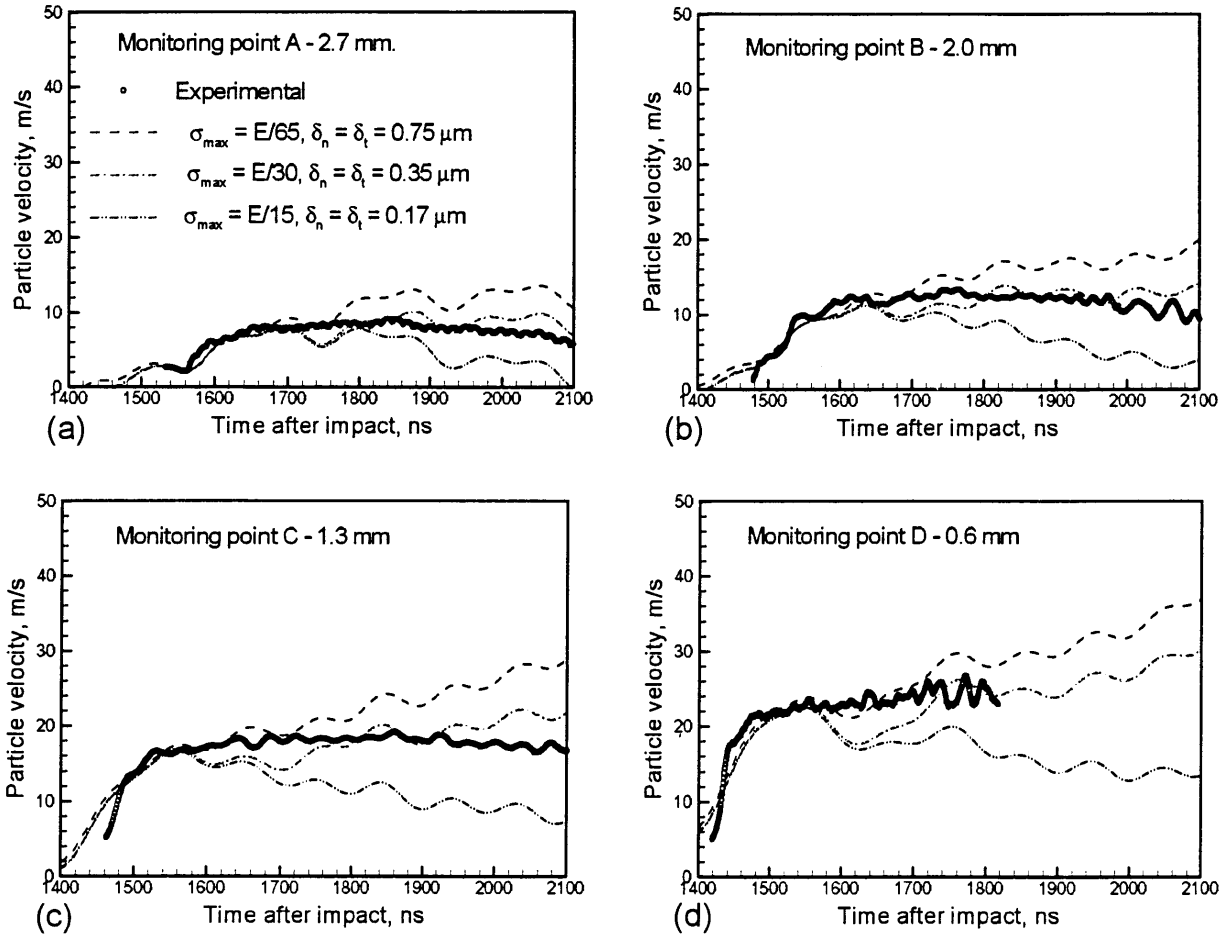

Fig. 9. Experimental and the computed free surface particle velocity history at the four monitoring points on the rear surface of the specimen. The computed profiles represent simulations of the experiment by employing three different cohesive surface parameter sets selected to model a range of material failure behavior from ductile to brittle. As observed from the plots, none of the cohesive surface parameter sets is able to simulate the experimentally measured free surface particle velocity profiles.

excess free surface particle velocity at all the four monitoring points, and at all times. On the other hand, the predictions for the free surface particle velocity history corresponding to the second data set are lower than the experimental profiles at all the four monitoring points, at all times. Thus, it can be argued that increasing the value of $\sigma_{\max}$ from $E/65$ to $E/15$ increases the material's resistance to crack growth even though the normal and the tangential characteristic lengths are decreased from 0.75–0.17 μm. This increase in material resistance leads to a lower crack tip acceleration, resulting in lower crack tip speeds and hence to a lower free surface particle velocity. This point was also noted by Varias and Shih (1993), who had reported that for the same level of material

toughness, it is the value of σ_{max} and not the characteristic length which dominates the failure of a cohesive surface.

In view of these aforementioned observations, a third set of cohesive surface parameters with $\sigma_{max} = E/30$ MPa and $\delta_n = \delta_t = 0.346$ μm is employed. This set of cohesive surface parameters model material failure behavior which is in between the ductile and cleavage fracture modes. Also, this set of cohesive surface parameters is consistent with $K_{IC} = 36\,\mathrm{MPa}\sqrt{\mathrm{m}}$. The computed free surface particle velocity history corresponding to this data set, at the four monitoring points, is shown by the dashed–dot line in Fig. (9a). Although, the computed profiles show a closer agreement with the experimental profiles at all the four monitoring points, the computed free surface particle velocities are lower than the experimental free surface particle velocity during the first-half of the time window and are in excess of the experimental profiles during the latter half.

From the results of these simulations it is seen that the cohesive surface model in its present form is not capable of predicting the dynamic crack growth observed in the low temperature experiment discussed here. By varying the cohesive surface parameters, the computed free surface particle velocity profiles can be made to agree with the experimental profiles either during the initial portion of the time window or the latter portion of the time window, but not for both. Thus, in order to capture the essential features of dynamic crack growth for the entire time window, it is necessary to introduce a means by which the energy required for decohesion increases with increasing cohesive-surface separation rate. It must be noted that this attribute of numerical modeling is consistent with the fractographs, which show an increase in inelastic deformation during the later part of crack growth.

4.2. Rate dependent cohesive surface model

In order to better model the experiments, especially the inelasticity occurring during the creation of the fracture surfaces a rate dependent cohesive surface model is sought. For simplicity, like in the case of the rate independent cohesive surface model, any dissipation accompanying the inelastic deformation is neglected. In this rate dependent cohesive surface model the normal cohesive strength is taken to be dependent on the instantaneous rate of normal separation, $\dot{\Delta}_n$, as

$$\sigma_{max}/\sigma^0_{max} = 1 + \beta\{\exp[\alpha(\dot{\Delta}_n/\dot{\Delta}^{ref}_n) - 1]\}, \tag{45}$$

where σ^0_{max} is the cohesive strength when $\dot{\Delta}_n = 0$; $\dot{\Delta}^{ref}_n$ is the reference of surface separation; and β and α are the parameters which control the growth of σ_{max} with $\dot{\Delta}_n$. Further, as for the case of the rate independent model, it is assumed that the normal component of the cohesive traction is not affected by the rate of tangential separation. In view of (45), it is anticipated that for very small opening rates, $\dot{\Delta}_n$, σ_{max} remains essentially unchanged from its rate independent value of σ^0_{max}. On the other hand, for rapid de-cohesion of the cohesive surfaces, the local magnitude of the cohesive stress is elevated by a magnitude determined by the ratio of the cohesive surface separation rate $\dot{\Delta}_n$, and the reference opening rate, $\dot{\Delta}^{ref}_n$.

The arguments for selecting a value for the reference opening rate, $\dot{\Delta}^{ref}_n$, are oblique at best. As an estimate of the reference opening rate within the yield zone, consider the crack tip opening

displacement δ, divided by the time required for the crack to advance one plastic zone length Λ, at speed v, that is

$$\dot{\Delta}_{\mathrm{n}}^{\mathrm{ref}} \approx \frac{\delta}{\Lambda/v}. \tag{46}$$

Under quasi-static conditions of small scale yielding

$$\Lambda = \frac{\pi}{8}\left(\frac{K_{\mathrm{I}}}{\sigma_0}\right)^2 \quad \text{and} \quad \delta = \frac{(1-\nu)}{2}\frac{K_{\mathrm{I}}^2}{\mu\sigma_0}. \tag{47}$$

Choosing $v = 1500$ m/s, the reference opening rate, $\dot{\Delta}_{\mathrm{n}}^{\mathrm{ref}}$, is approximately equal to 30 m/s.

Figure 10(a) shows the maximum normal cohesive strength as a function of the cohesive surface separation rate for $\alpha = 1.6$. The model parameters α and β govern the rate sensitivity of the maximum cohesive stress to the cohesive surface separation rate $\dot{\Delta}_{\mathrm{n}}$, with $\beta = 0$ providing the rate independent limit. Figure 10(b) shows the variation of the normalized normal cohesive traction $T_{\mathrm{n}}/\sigma_{\max}^0$, with the normalized normal displacement $\Delta_{\mathrm{n}}/\delta_{\mathrm{n}}$, for various values of the ratio $\dot{\Delta}_{\mathrm{n}}/\dot{\Delta}_{\mathrm{n}}^{\mathrm{ref}}$. As expected the are under the traction–displacement increases considerably with the increase in the normal surface separation rate, $\dot{\Delta}_{\mathrm{n}}$. The increase in area represents the extra energy that is required for decohesion of the fracture surfaces at the elevated surface separation rates. The curve with $\dot{\Delta}_{\mathrm{n}}/\dot{\Delta}_{\mathrm{n}}^{\mathrm{ref}} = 0$ (rate independent limit) is similar to the one employed by Xu and Needleman (1994) in their simulations of dynamic failure of brittle materials.

The predictions of the free surface particle velocity of the target plate for the rate dependent cohesive surface model with $\sigma_{\max} = E/65$ MPa, $\delta_{\mathrm{n}} = \delta_{\mathrm{t}} = 0.75$ μm, $\beta = 0.05$, and $\alpha = 1.6$, are represented by the solid lines shown in Figs 11(a)–(d). Unlike, for the case of the rate independent cohesive surface model discussed in Section 4.1, for the rate dependent cohesive surface model the agreement between the computed and the measured free surface particle velocity history is observed to be satisfactory for the entire time duration of interest.

Figures 12(a) and (b) show the normal component of the cohesive surface traction and the normal surface separation rate as a function of normal displacement jump across the cohesive surface, at two different distances from the initial crack tip location. As expected, for the rate dependent cohesive surface model the normal component of the cohesive surface traction does not fall with an increase in the cohesive surface separation after $\Delta_{\mathrm{n}}/\delta_{\mathrm{n}} = 1$ (as was observed for the rate independent case ($\beta = 0$)). Instead, the normal cohesive traction increases with the increase in the normal component of the cohesive surface separation rate, $\dot{\Delta}_{\mathrm{n}}$. This increase in the normal component of the cohesive surface traction results in the shift in the location of the peak normal surface traction from $\Delta_{\mathrm{n}}/\delta_{\mathrm{n}} = 1$ to approximately $\Delta_{\mathrm{n}}/\delta_{\mathrm{n}} = 2$. This change in the location of the peak results in additional energy being required for decohesion during the material fracture process, especially during the relatively high cohesive-surface separation rates observed during dynamic fracture towards the latter part of crack growth. A similar trend is observed at a point located 400 μm from the initial position of the crack tip on the prospective crack path (Fig. 12(b)).

4.2.1. Location of crack tip and estimation of the crack tip speed

To calculate the crack tip location and consequently the crack tip speed in the aforementioned dynamic fracture simulations the following algorithm is used: initially, there is a well-defined crack

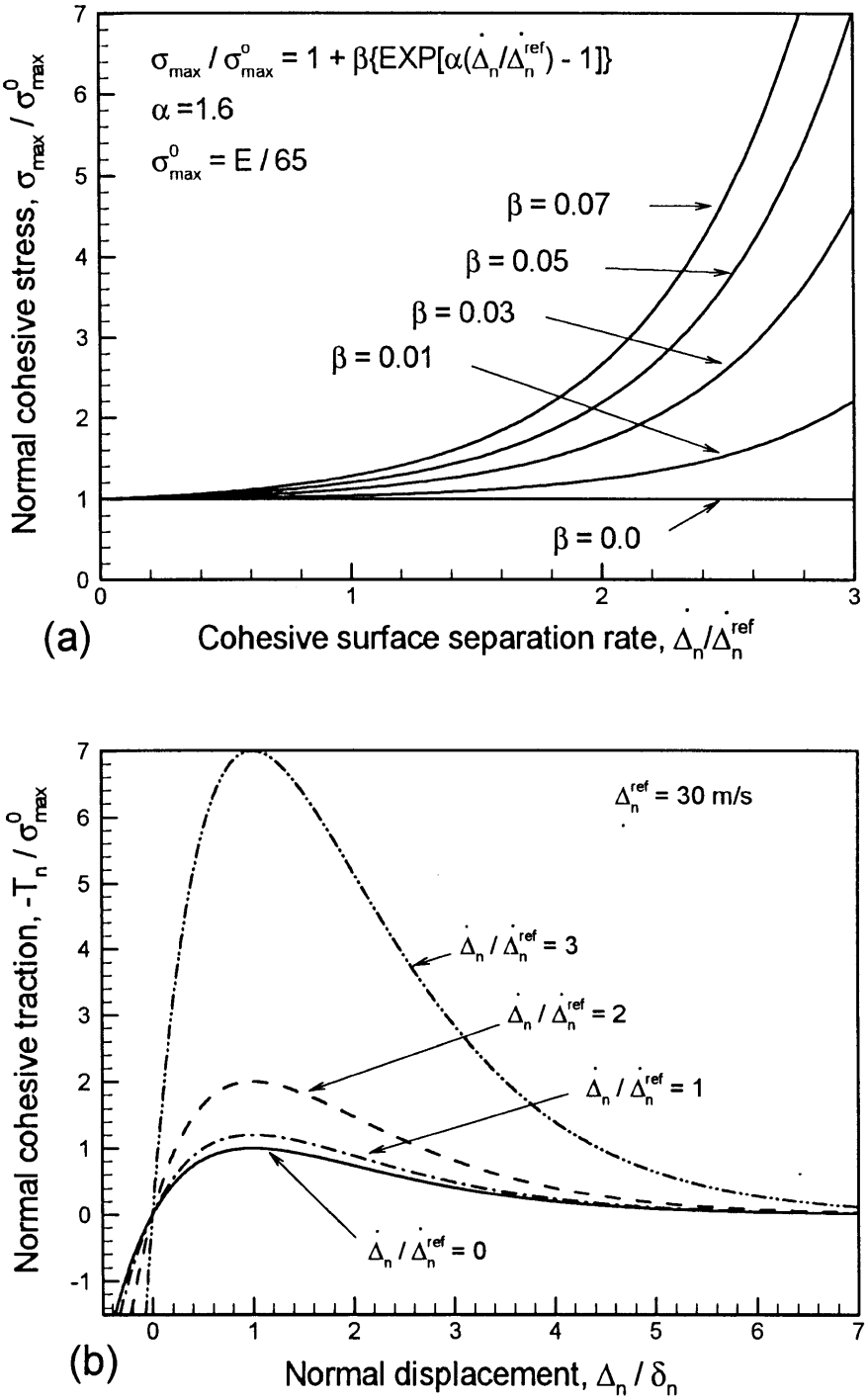

Fig. 10. Features of the rate-dependent cohesive surface model. (a) Variation of maximum cohesive surface strength σ_{max}, as a function of the normalized cohesive surface separation rate, for various values of the parameter β. $\beta = 0$ represents the rate-independent limit. (b) Normal cohesive surface traction as a function of the normalized normal displacement across the cohesive surfaces (with $\Delta_t = 0$), for various cohesive surface separation rates.

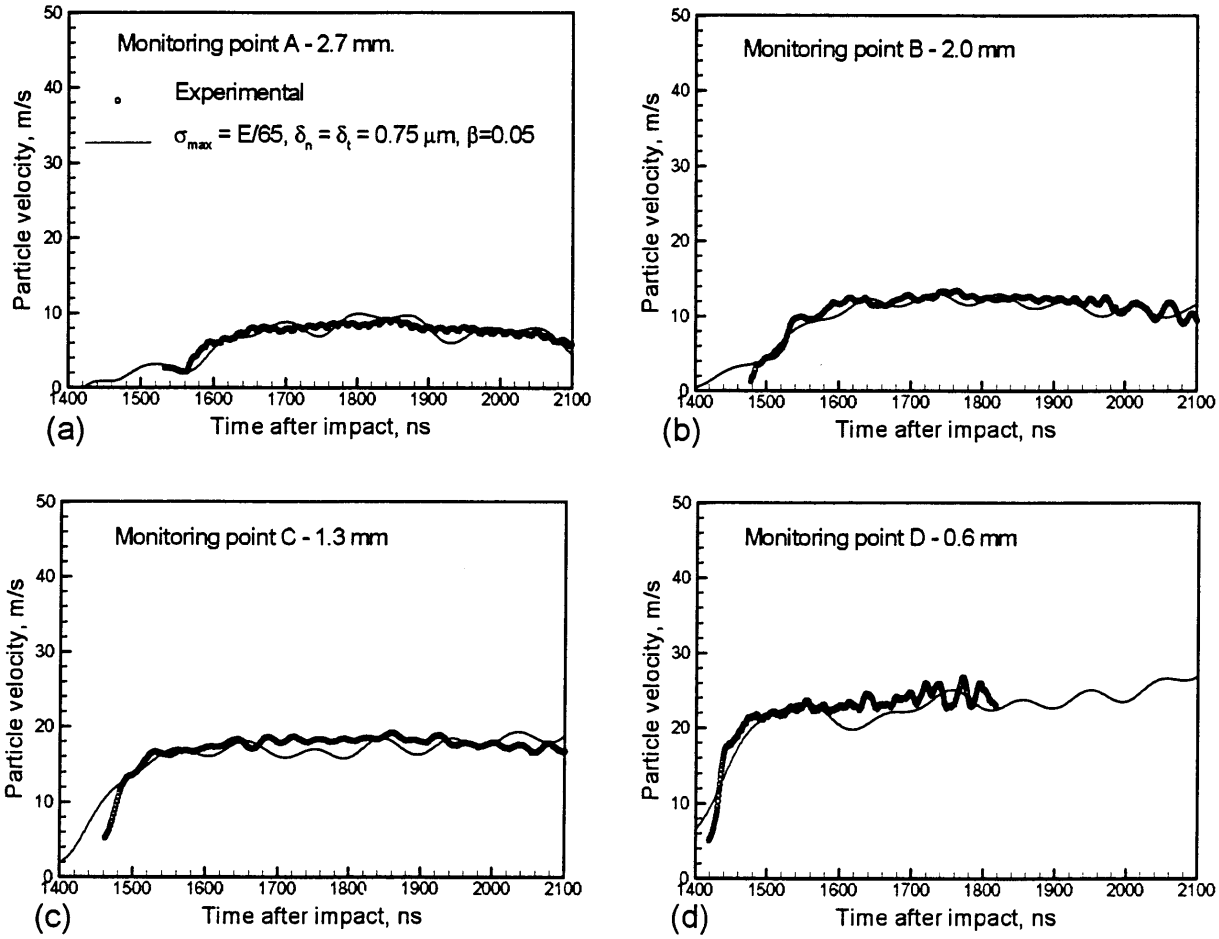

Fig. 11(a–d). Experimental and computed free-surface particle velocity vs time profiles for the rate dependent cohesive surface model. Unlike the rate independent cohesive surface model, the rate dependent cohesive surface model is capable of simulating the measured free surface particle velocity history at all the four monitoring points.

tip location, namely the terminus of the interval over which $\sigma_{\max} = \tau_{\max} = 0$. Once the crack initiates, this is no longer the case because of the continuous dependence of the cohesive surface tractions on the displacement jump, Δ_n. For presentation of results, the largest value of y^1 for which $\Delta_n \geqslant 10\delta_n$ is recorded together with the current time. This value of y^1 is denoted as a and is identified with the current crack tip position. A polynomial curve is fit through five points of the a vs t curve, and the slope of this polynomial is taken to be the current crack tip speed, $\dot{a}_n$, at t_n. Some numerical experiments were carried out using other values of Δ_n to define the crack location, e.g. $3\delta_n$ or $7\delta_n$, and the predictions of the crack location and the crack speed were not very sensitive to the precise choice. Figure 13 shows the history of crack growth and the crack tip speed corresponding to rate dependent cohesive surface model. The crack tip speed increases continuously during the initial 450 ns after the arrival of the loading pulse at the crack plane, after which it

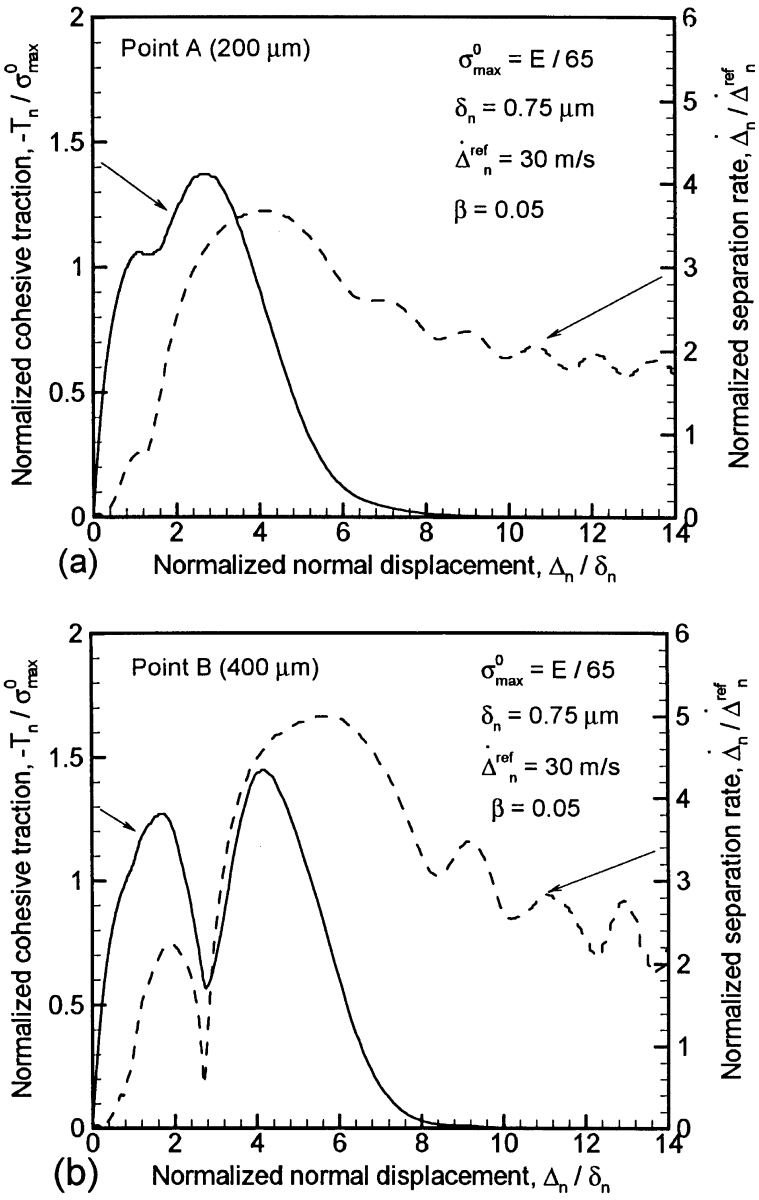

Fig. 12. (a) History of the cohesive surface traction and the cohesive surface separation rate as a function of the normal surface displacement, at a point 200 μm ahead of the initial crack tip. (b) History of the cohesive surface traction and the cohesive surface separation rate as a function of the normal surface displacement, at a point 400 μm ahead of the initial crack tip. Note that the normal cohesive surface tractions do not reach a maximum at $(\Delta_n/\delta_n) = 1$, as was the case in the rate independent cohesive surface model.

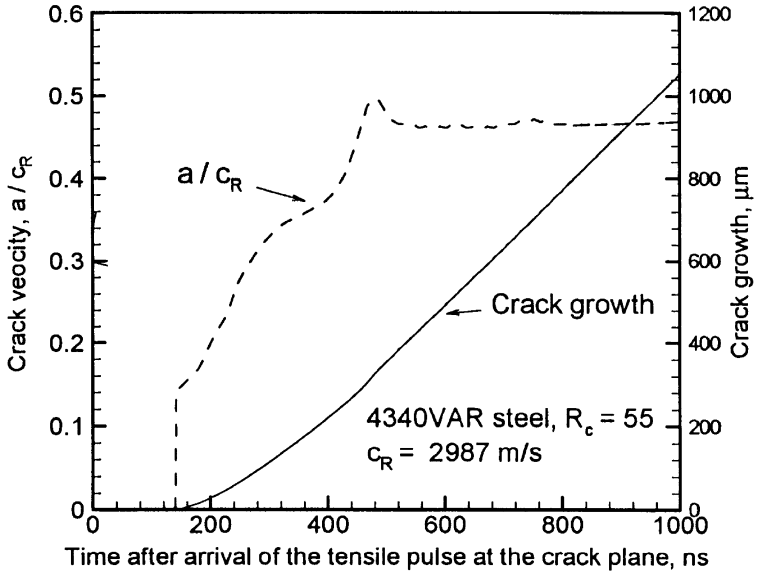

Fig. 13. History of crack growth and the crack tip speed for the rate dependent cohesive surface model.

reaches a plateau at approximately 1400 m/s (which corresponds to approximately 45% of the elastic Rayleigh wave speed). The total crack growth occurring during the 1 μs loading duration is approximately 1.3 mm and corresponds well with the experimentally measured crack growth.

4.2.2. Dynamic material toughness vs crack tip speed relationship for 4340*VAR steel at* $-80^{\circ}C$.

Results of several dynamic fracture experiments on tough structural metals which do not undergo a transition in fracture mode with increasing crack tip speed and show relatively low strain hardening characteristics in the plastic range, indicate that the material's level of resistance to crack advance may depend on the instantaneous crack tip (see, e.g. Rosakis et al., 1984; Rosakis and Zhender, 1990; Kobayashi and Dally, 1979). In particular, as suggested by Kanninen and Popelar (1985), experimental data of Rosakis et al. (1984) on dynamic fracture of 4340 steel, can be correlated by the heuristic experimental relation

$$K_{\mathrm{ID}}(t,\dot{a}) = \frac{K_{\mathrm{Ic}}}{1-\left(\dfrac{\dot{a}}{V_{\mathrm{L}}}\right)^{m}}. \tag{48}$$

In (48), K_{Ic} is the crack initiation toughness under dynamic loading conditions; V_{L} is the limiting crack tip speed; and m is a dimensionless shape factor. Using (48), the K_{ID} vs $\dot{a}$ curve for 4340 steel (heated to 843°C, oil quenched and tempered at 316°C for an hour, and with $\sigma_0 = 1300$ MPa and $K_{\mathrm{Ic}} = 60\,\mathrm{Mpa}\sqrt{\mathrm{m}}$), can be effectively represented with $V_{\mathrm{L}} = 1100$ m/s and $m = 2$.

The most significant feature of this K_{ID} vs $\dot{a}$ relationship [equation (48)] is the increasing sensitivity of the dynamic fracture toughness to crack-tip speed with increasing speed. Although

this sensitivity might be attributed, at least in part, to strain rate dependence of the material response, it is noteworthy that the feature persists even for materials which appear to exhibit little strain rate dependence in their bulk response. Furthermore, the feature cannot be attributed entirely to crack speed dependence of the elastic field surrounding the crack tip plastic zone. The surrounding elastic field shows little dependence on crack speed for speeds less than about 50–60% of the shear wave speed, whereas the sharp upturn in the variation of toughness with speed has been observed for speeds in the range of 25–30% of the shear wave speed. Theoretical/numerical investigations of dynamic fracture in elastic ideally–plastic materials (Lam and Freund, 1985) have shown that this upturn in the material's fracture resistance can be attributed to inertial effects within the crack tip plastic zone. Furthermore, it has been demonstrated that for ductile solids, the inertia effects become important at much lower crack tip speeds as compared to those in brittle solids.

In order to estimate the dynamic material toughness vs crack tip relationship for the 4340VAR steel at lower than room temperature (test temperature -80°C), the J-integral is evaluated as a function of time. The J-integral employed is the generalization of Rice's J-integral (Rice, 1968) to dynamic conditions, which involves a contour integral as well as an integral over the area inside the contour (Moran and Shih, 1987; Nakamura et al., 1985):

$$J = \int_{\Lambda} [(W+L)\,\mathrm{d}y^2 - T^i u_{i,1}\,\mathrm{d}s] + \int_A \left[\partial \tau_k^k T_{,1} + \rho \frac{\partial^2 u^i}{\partial t^2} u_{i,1} - \rho \frac{\partial u^i}{\partial t}\left(\frac{\partial u_i}{\partial t}\right)_{,1}\right] \mathrm{d}A, \tag{49}$$

where A is the area of the contour Γ and

$$W = \int_0^{E_{ij}} \tau^{ij}\,\mathrm{d}E_{ij} - \alpha \int_0^T \tau_k^k\,\mathrm{d}T, \quad L = \frac{1}{2}\rho \frac{\partial u^i}{\partial t}\frac{\partial u_i}{\partial t}. \tag{50}$$

Using (50), J is computed on several contours ignoring any contribution of the cohesive surfaces. The deviation on all paths away from the uniform mesh was within 5%, with the deviation being less in the early stages of crack growth.

Figures 14(a) and (b) show the computed profiles for the J-integral and COD (crack opening displacement) vs time for the rate dependent cohesive surface model. Along with these curves, the J-integral and the COD profiles for the case of the stationary crack are also shown for comparison purposes. Prior to the onset of crack growth the curves of COD and the J-integral increase monotonically as predicted by the elastodynamic solution for a half plane stationary crack subjected to plane tensile pulse [eqns (1)–(3)]. With the onset of crack extension the COD grows linearly and exceeds the COD level for the case of stationary crack. The J-integral also increases with the crack growth but its value is always lower than that obtained for the case of stationary crack. This is to be expected since the universal function for the energy release rate, $G(v)$ (Freund, 1990), decrease monotonically with the increase in crack tip speed. Crack growth is observed to begin at approximately 6 KJ/m^2, which is about 3–4% below ϕ_n at crack initiation.

Figure 15 shows the normalized dynamic fracture roughness vs dimensionless crack tip speed for the low temperature dynamic fracture of 4340VAR steel ($R_c = 55$), obtained using the rate-dependent cohesive surface model in the present investigation, along with the room temperature dynamic fracture of 4340 steel ($R_c = 45$) obtained by using (48). Both steels show a monotonically

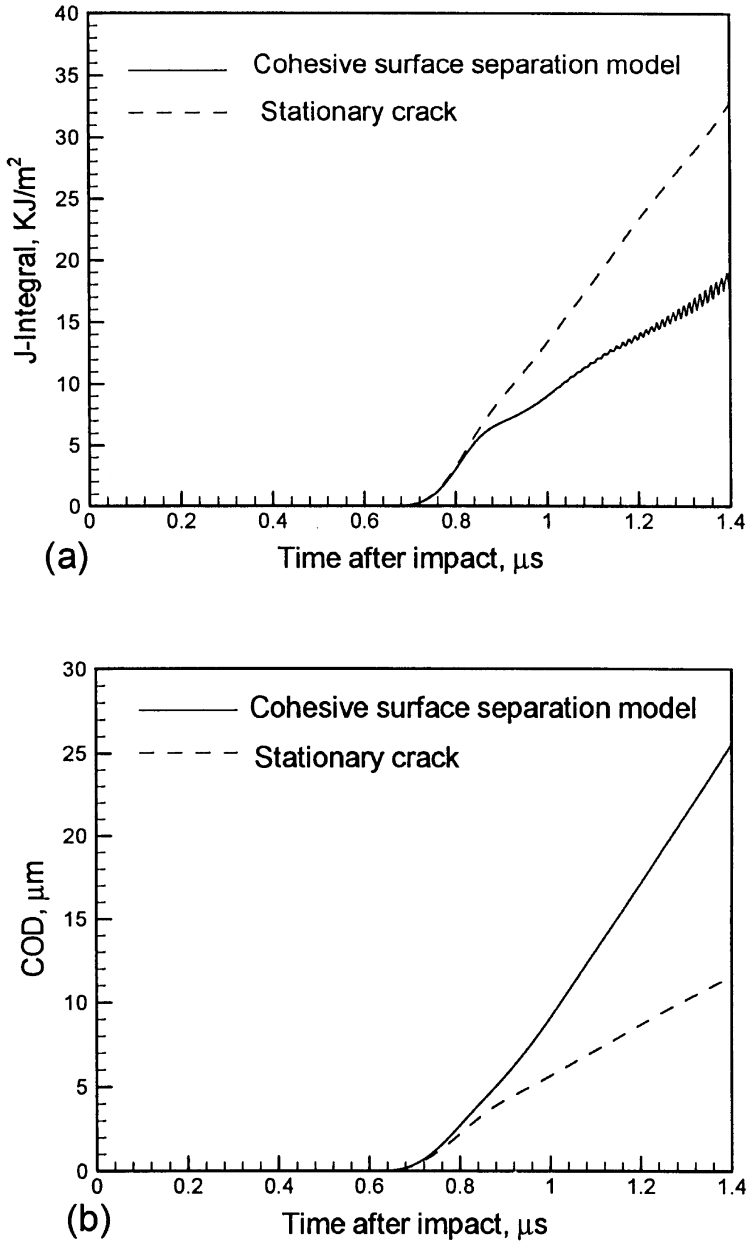

Fig. 14. (a) *J*-integral vs time profile for dynamic crack growth corresponding to the rate dependent cohesive surface model, compared with the *J*-integral history for the stationary crack. Note up to the time of crack initiation, the *J*-integral for the stationary crack and the dynamic crack growth are in agreement. After crack initiation the *J*-integral for the two cases deviate from each other. (b) COD vs time profile for the stationary crack and for dynamic crack growth. Again up to the time of crack initiation the COD for the stationary crack and dynamic crack growth are in agreement. At the moment of crack initiation the COD for the two cases deviate from each other.

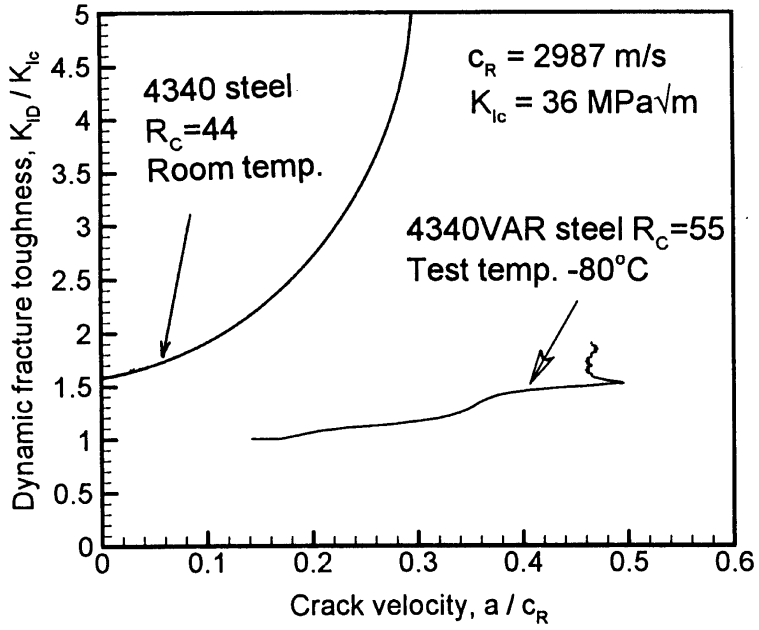

Fig. 15. Normalized dynamic fracture toughness vs crack tip speed for the room temperature dynamic fracture of 4340VAR steel ($R_c = 45$) and the low temperature dynamic fracture of 4340VAR steel ($R_c = 55$).

increasing fracture toughness vs crack velocity relationship which takes on large values for moderate values of $\dot{a}/c_R$ ratio. Although there is no unambiguous way to associate a terminal velocity with these results, the plot suggests a maximum attainable velocity well below the Rayleigh wave speed of the material. The intercept value of fracture toughness at $\dot{a}/c_R = 0$ corresponds to the so-called steady state toughness value of the theory of stable crack growth. The spread of intercepts on the $\dot{a}/c_R = 0$ results because of the normalization factor (K_{Ic} corresponding to the 4340VAR steel ($R_c = 55$) at -80°C) used to normalize all data shown on the plot. As discussed by Lam and Freund (1985), the variation of fracture toughness with crack speed for 4340 steel with $R_c = 45$ is primarily due to inertial effects. It is anticipated that if the inertial effects were neglected, the calculated toughness would be completely independent of speed (Seigmond and Needleman, 1997). This observation is also consistent with the analysis of Mataga et al. (1987), who using a strain-based crack growth criterion have shown that in tough ductile structural steels, the upturn in the material fracture resistance occurs at relatively lower crack tip speeds as compared to more brittle materials.

4.2.3. Energy partitioning during the dynamic fracture process

Energy partitioning provides another perspective on the coupled thermo-material processes occurring during the dynamic fracture process. Since the cohesive surface relationship is considered to be elastic, only the dissipative mechanisms associated with the volumetric viscoplastic deformation are considered. The work done by the imposed loading can be expressed as

$$\int_{S_{\text{ext}}} \mathbf{f}\cdot\dot{\mathbf{u}}\,\mathrm{d}S = \frac{\mathrm{d}}{\mathrm{d}t}\int_v \frac{1}{2}\rho_0\dot{\mathbf{u}}\cdot\dot{\mathbf{u}}\,\mathrm{d}V + \int_v \boldsymbol{\tau}:\mathbf{D}\,\mathrm{d}V + \frac{\mathrm{d}}{\mathrm{d}t}\int_{S_{\text{int}}} \phi\,\mathrm{d}S. \tag{51}$$

This identity specifies the balance between the rates at which the mechanical work is performed through the specimen boundary, the rate of change of kinetic energy in the specimen, the stress power, and the rate at which energy is being stored in the cohesive surfaces. The stress power consists of an elastic part, a plastic part and a thermal part, i.e.,

$$\int_v \boldsymbol{\tau}:\mathbf{D}\,\mathrm{d}V = \int_v \boldsymbol{\tau}:\mathbf{D}^{\text{e}}\,\mathrm{d}V + \int_v \boldsymbol{\tau}:\mathbf{D}^{\text{p}}\,\mathrm{d}V + \int_v \alpha\dot{T}\boldsymbol{\tau}:\mathbf{I}\,\mathrm{d}V. \tag{52}$$

Integrating (51) in time yields

$$\int_0^t\int_{S_{\text{ext}}} \mathbf{f}\cdot\dot{\mathbf{u}}\,\mathrm{d}S = \int_v \frac{1}{2}\rho_0\dot{\mathbf{u}}\cdot\dot{\mathbf{u}}\,\mathrm{d}V + \int_0^t\int_v \boldsymbol{\tau}:\mathbf{D}\,\mathrm{d}V + \int_{S_{\text{int}}} \phi\,\mathrm{d}S \tag{53}$$

where $P(t) = \int_0^t\int_{S_{\text{ext}}}\mathbf{f}\cdot\dot{\mathbf{u}}\,\mathrm{d}S$, is the total work done by the imposed boundary tractions upto time t, $K(t) = \int_v \frac{1}{2}\rho_0\dot{\mathbf{u}}\cdot\dot{\mathbf{u}}\,\mathrm{d}V$ is the current kinetic energy of the specimen, $W(t) = \int_0^t\int_v \boldsymbol{\tau}:\mathbf{D}\,\mathrm{d}V$ is the accumulated stress work upto time t, and $\psi(t) = \int_{S_{\text{int}}}\phi\,\mathrm{d}S$ is the current cohesive energy stored in the cohesive surfaces.

Figure 16(a) shows how the energy represented by each term in (52) varies as a function of time for the rate dependent cohesive surface model with $\sigma_{\max} = E/65$ MPa, $\delta_{\text{n}} = \delta_{\text{t}} = 0.75\ \mu$m, $\beta = 0.05$, and $\alpha = 1.60$. In the early stages of the loading, there is relatively equal partitioning of the boundary work into kinetic and elastic strain energy. As the stress wave reaches the crack plane, the kinetic energy increases at the expense of strain energy. The undulations observed in the kinetic energy, thereafter, are a consequence of the diffracted waves which are produced during the interaction of the plane tensile pulse with the traction-free crack-faces and the refraction of the waves from the free surface of the specimen and the lateral surfaces of the specimen due to its finite dimensions. During the entire duration of the loading pulse the cohesive energy, the thermal energy and plastic work are negligible in comparison with either the kinetic energy or the elastic strain energy. As a check, the sum of the kinetic energy, the elastic strain energy, the thermal work, the plastic dissipation, and the cohesive energy, to a very good approximation, is equal to the work done by the boundary loading.

The relative magnitudes of the plastic dissipation $\int\boldsymbol{\tau}:\mathbf{D}^{\text{p}}\,\mathrm{d}t$, and the cohesive surface energy $\int_{s_{\text{int}}}\phi\,\mathrm{d}s$, are plotted as a function of time after impact in Fig. 16(b). The energy values in Fig. 16(b) pertain to the entire specimen with a meter thickness. Upon the arrival of the tensile loading pulse at the crack plane the cohesive energy increases monotonically for the entire duration of the loading. The plastic dissipation is negligible for the initial 200 ns after the arrival of the tensile wave at the crack plane, but increases steadily at the latter times. This behavior is also consistent with the mode of failure observed during crack growth. In the initial stages of quasi-cleavage failure fracture occurs by a predominantly cleavage mode. But as crack growth progresses, the crack tip accelerates leading to the elevation of the material's cohesive strength due to its dependence on the rate of separation of the cohesive surfaces. This increase in the material's cohesive strength leads to an increase in the ratio of $\sigma_{\max}/\sigma_0$ and hence an increase in the fraction of inelastic deformation accompanying the decohesion of the fracture surfaces.

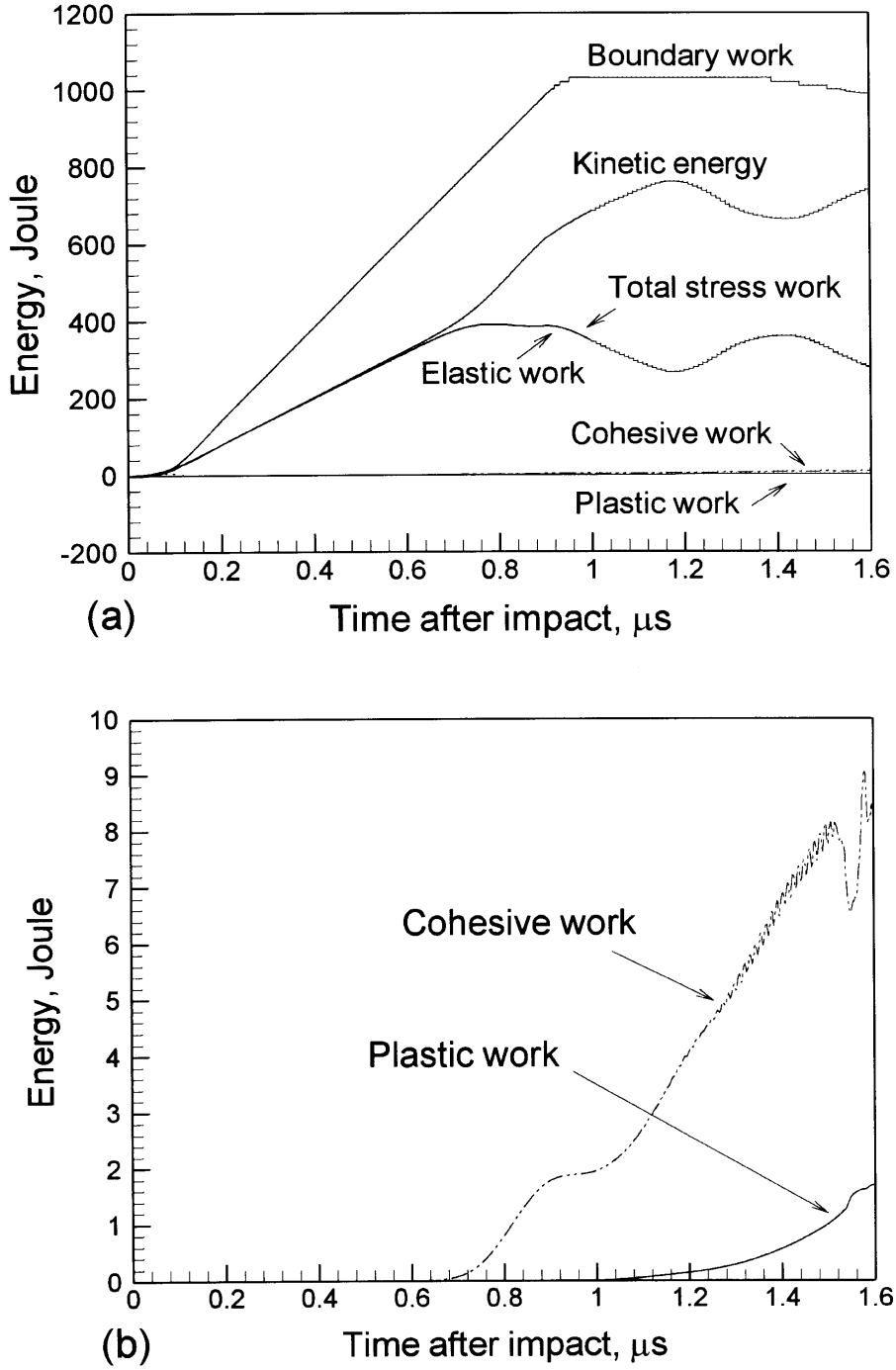

Fig. 16. (a) Energy balance for the rate dependent cohesive surface model. (b) Comparison of the accumulated plastic work and the current elastic energy stored in the cohesive surfaces.

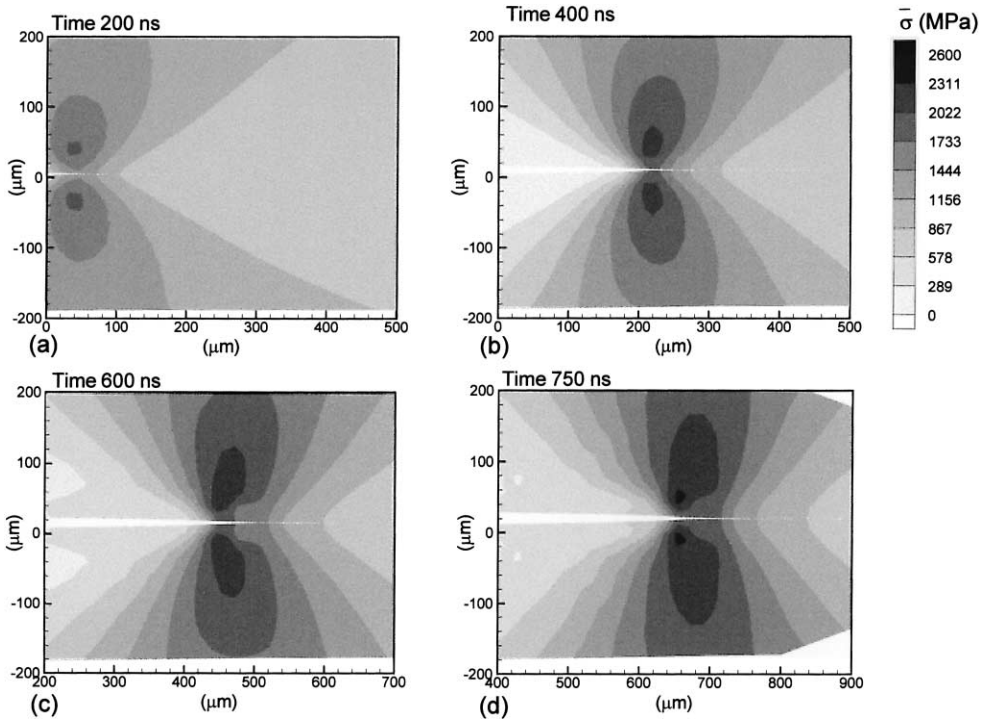

Fig. 17. Contours of the von Mises effective stress in the vicinity of the propagating crack at time (a) $t = 200$ ns, (b) $t = 400$ ns, (c) $t = 600$ ns and (d) $t = 750$ ns, after the arrival of the tensile wave tip at the crack plane. Note that the contour plots show a maximum just behind the leading crack tip. This illusion is an artifact of the cohesive surface modeling of crack growth in which the crack tip appears to be longer than it actually is.

4.2.4. Local distribution of von Mises stress, effective plastic strain, temperature, effective plastic strain rate, and effective elastic strain rate

Contours of von Mises effective stress in the vicinity of the crack tip, are shown in Fig. 17(a)–(d) at four different time intervals after the arrival of the tensile wave at the crack plane. For the contour plots at $t = 200$ ns and $t = 400$ ns the contours of effective von Mises stress are similar in shape and level to those for the elastic material. At later times (contour plots at $t = 600$ ns and $t = 750$ ns), the crack tip accelerates resulting in an increase in the cohesive surface separation rate. The increase in the cohesive surface separation rate leads to a $\sigma_{\max}/\sigma_0$ ratio of greater than unity. This relatively high level of cohesive strength as compared to the flow strength of the surrounding material leads to noticeable plastic deformation in the vicinity of crack faces. This can also be inferred from the shape of the von Mises effective stress contours which show a region of enhanced von Mises effective stress behind the crack tip. Also, it is noted that the contour plots for the effective von Mises stress show a maximum just behind the leading crack tip. This illusion is an artifact of the cohesive surface model employed to simulate crack growth, in which the crack tip appears to be longer than it actually is. As discussed in Section 4.2.1, even though the crack faces appear to be separated at the crack tip, the crack faces in the vicinity of the crack tip are not

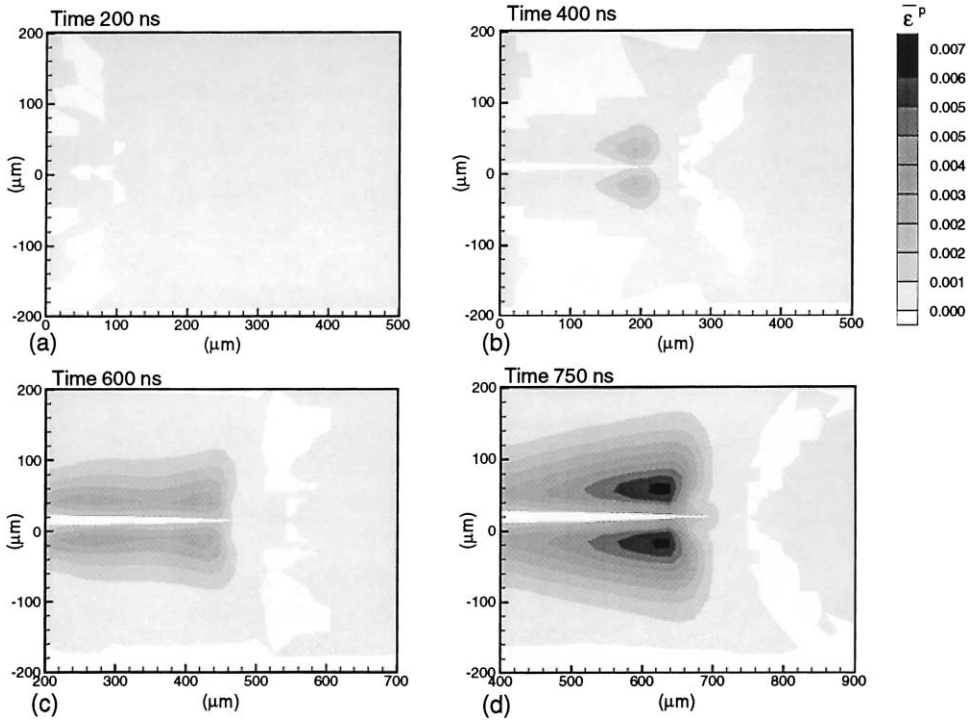

Fig. 18. Contours of the effective plastic strain in the vicinity of the propagating crack at time (a) $t = 200$ ns, (b) $t = 400$ ns, (c) $t = 600$ ns and (d) $t = 750$ ns, after the arrival of the tensile wave tip at the crack plane. The equivalent plastic strain in the vicinity of the crack tip increases with the crack growth (to a maximum of 0.7% plastic strain).

traction free. The crack faces become traction free only after the normal and tangential separation reach a certain pre-defined critical value. In the present simulations the actual crack tip location is taken to be the position where the crack tip opening displacement is greater than $5–7\delta_n$.

Figure 18(a)–(d) and 19(a)–(d) show contour plots for the effective plastic strain, $\bar{\varepsilon}^p$, and temperature distribution in the vicinity of the crack tip, at four different time intervals after the arrival of the tensile wave at the crack plane. The equivalent plastic strain in the vicinity of the crack tip increase with the crack growth (to a maximum of 0.7% plastic strain). Also, the plastic strain profiles show decreasing plastic strain with increasing distance from the crack tip, in the wake region behind the crack tip. The temperature change in the vicinity of the crack tip is very small. It increases from -80°C to -76°C during the entire duration of the experiment. The temperature contours, which are similar to the equivalent plastic strain contours, indicate that the heating extends in a narrow region around the crack tip and the deformation remains essentially adiabatic in the wake region behind the crack tip.

During rapid crack growth the strain rates experienced by a material particle in the path of an advancing crack are potentially enormous. It is understood that the essence of cleavage crack growth in elastic–viscoplastic material is the ability to elevate the stress to a critical level before plastic flow can accumulate to defeat the influence of the crack-tip. In terms of the mechanical

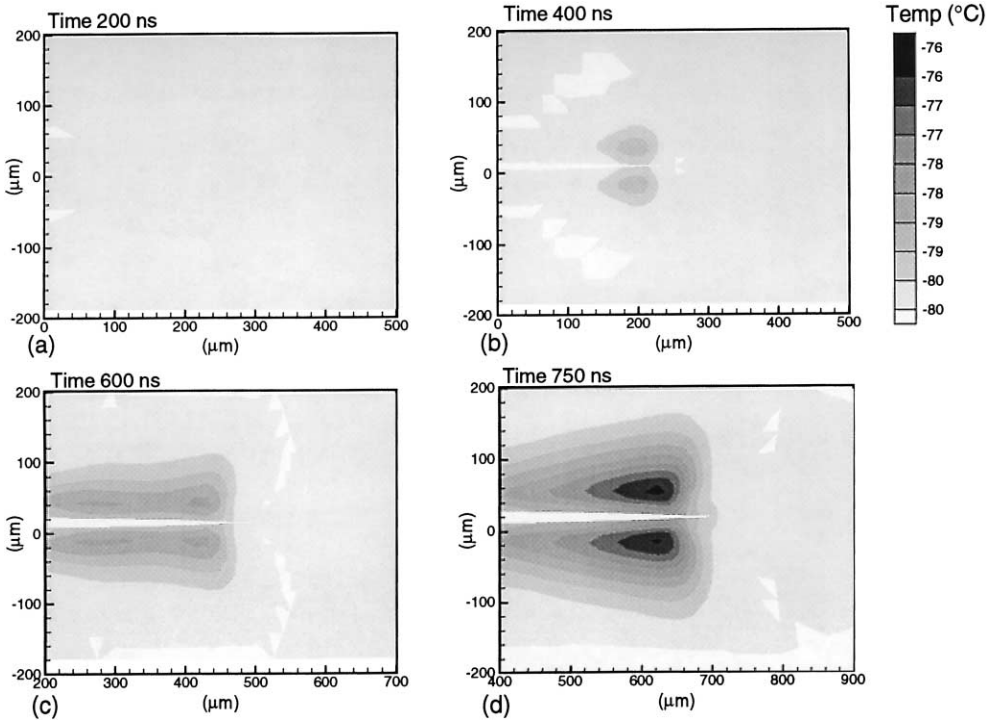

Fig. 19. Contours of the local temperature in the vicinity of the propagating crack at time (a) $t = 200$ ns, (b) $t = 400$ ns, (c) $t = 600$ ns and (d) $t = 750$ ns, after the arrival of the tensile wave tip at the crack plane. The temperature change in the vicinity of the crack tip is very small. It increases from -80–76°C during the entire duration of crack growth.

fields near the edge of an advancing crack, the rate of stress increase is determined by the elastic strain-rate, while the rate of crack-tip blunting is determined by the plastic strain-rate. Figures 20 and 21 show the contour plots for the effective elastic strain rate, $\dot{\bar{\varepsilon}}^{e}$ (defined as $\sqrt{3\mathbf{D}^{e}:\mathbf{D}^{e}/2}$) and the effective plastic strain rate $\dot{\bar{\varepsilon}}^{p}$, respectively, in the vicinity of the crack tip at four different time intervals after the arrival of the tensile wave at the crack plane. As can be seen from the contour plots, the effective elastic strain rates dominate the effective plastic strain rates during the initial time period of crack growth, after which the effective elastic strain rates are of the same order as the effective plastic strain rates. This behavior is consistent with the predominantly cleavage mode of failure observed during the early crack growth time period, and the increase in inelastic deformation with crack growth during the later times.

5. Conclusions

In the present investigation, results of plate impact dynamic fracture experiments conducted at lower than room temperature (-80°C), along with finite element modeling is employed to study the validity of cohesive surface models in predicting fast fracture dynamics in high strength

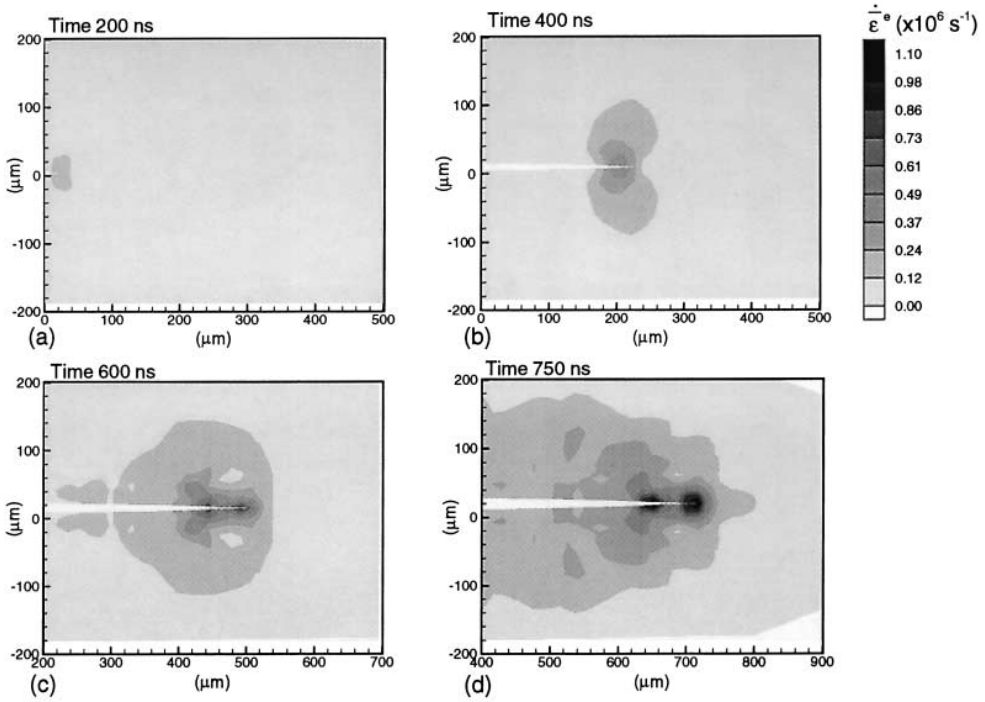

Fig. 20. Contours of the effective elastic strain rates in the vicinity of the propagating crack at time (a) $t = 200$ ns, (b) $t = 400$ ns, (c) $t = 600$ ns and (d) $t = 750$ ns, after the arrival of the tensile wave tip at the crack plane.

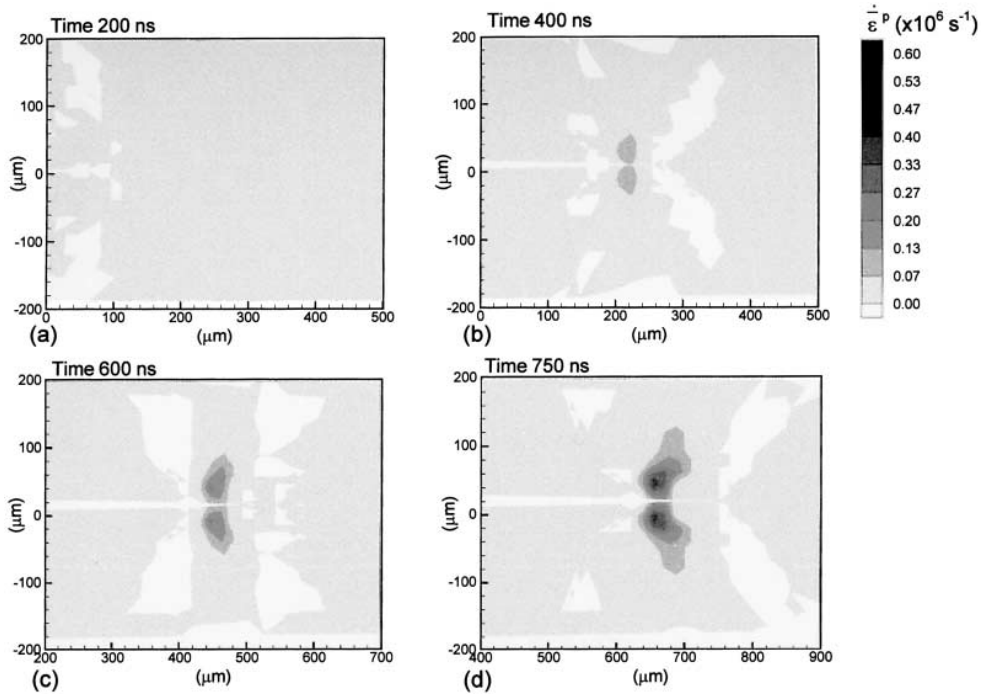

Fig. 21. Contours of the effective plastic strain rate in the vicinity of the propagating crack at time (a) $t = 200$ ns, (b) $t = 400$ ns, (c) $t = 600$ ns and (d) $t = 750$ ns, after the arrival of the tensile wave tip at the crack plane.

structural steels. From the results of these simulations it is observed that the cohesive surface models which employ a constant cohesive surface strength and a characteristic length, are not capable of capturing the dynamic fracture characteristics of fast fracture occurring in high strength structural steels. However, the results of the simulations are in reasonably good agreement with the experimental measurements when the cohesive surface model includes a work of separation which depends on the cohesive-surface separation rate. Moreover, the dynamic material toughness inferred from computational results, emphasize the existence of a sharp upturn in dynamic fracture toughness at a material characteristic limiting crack tip speed even at test temperatures as low as -80°C and under ultra-high crack-tip loading rates, $\dot{K}_{\mathrm{I}} = 10^{8}$ MPa$\sqrt{\mathrm{m}}$/s.

Acknowledgement

The computations reported in the manuscript were carried out on the Cray-YMP8 8/128 at the Ohio Supercomputer Center.

References

Achenbach, J.D., Nuismer, R., 1971. Fracture generated by dilational wave. International Journal of Fracture 7, 77–88.

Ahmad, J., Jung, J., Barnes, C.R., Canien, M.F., 1983. Elastic–plastic finite element analysis of dynamic fracture. Engineering Fracture Mechanics 17, 235–246.

American Society of Testing and Materials, 1965. Plane strain crack toughness testing of high strength metallic materials. In: Brown, W.F.J., Srawley, J.E. (Eds.), ASTM STP 410.

American Society of Testing and Materials, 1970. Review of developments in plane strain fracture toughness testing. In: Brown, W.F.J. (Ed.), ASTM STP 463.

Belytschko, T., Chiapetta, R.L., Bartel H.D., 1976. Efficient large scale non-linear transient analysis by finite elements. International Journal of Numerical Methods in Engineering 10, 579–596.

Brickstad, B., Nilson, 1980. Numerical evaluation by FEM of crack propagation experiments. International Journal of Fracture 16, 71–84.

Broberg, K.B., 1979. On the behavior of the process region at a fast running crack tip. In: Kawata, K., Shioiri J. (Eds.), High Velocity Deformation of Solids. Springer, Berlin Heidelberg, pp. 182–194.

Budiansky, B., 1969. Remarks on theories of solid and structural mechanics: problems of hydrodynamics and continuum mechanics. In: Lavrent'ev, M.A. et al. (Eds.), SIAM, pp. 77–83.

Campbell, J.D., Ferguson, W.G., 1970. The temperature and strain rate dependence of the shear strength of mild steel. Philosophical Magazine 21, 63–82.

Clifton, R.J. 1990. High strain rate behavior of metals. Applied Mechanics Reviews 43, S10–S22.

Freund, L.B., 1973. Crack propagation in an elastic solid subjected to general loading. III. Stress wave loading. Journal of the Mechanics and Physics of Solids 21, 47–61.

Freund, L.B., 1990. Dynamic fracture mechanics. Cambridge University Press, Cambridge, U.K.

Freund, L.B., Hutchinson, J.W., 1985. High strain rate crack growth in rate dependent plastic solids. Journal of the Mechanics and Physics of Solids 33, 169–191.

Hoff, R., Rubin, C.A., Hahn, G.T., 1991. Visco-plastic finite element analysis of rapid fracture. Engineering Fracture Mechanics 26, 445–461.

Johnson, E., 1992. Process region changes for rapidly propagating cracks. International Journal of Fracture 55, 47–63.

Johnson, E., 1993. Process region influence on energy release rate and crack tip velocity during rapid crack propagation. International Journal of Fracture 61, 183–187.

Kannien, M.F., Popelar, C.H., 1985. Advanced Fracture Mechanics. Oxford University Press, New York, Oxford.

Klopp, R.W., Clifton, R.J., Shawki, T.G., 1985. Pressure-shear impact and the dynamic plastic response of metals. Mechanics of Materials 4, 375–385.

Kobayashi, T., Dally, J.W., 1979. Crack arrest methodology and applications. In: Hahn, G.T., Kanninen, M.F. (Eds.), ASTM STP 711. American Society of Testing and Materials, Philadelphia, pp. 189–210.

Krieg, R.D., Key, S.W., 1973. Transient shell response by numerical time integration. International Journal of Numerical Methods in Engineering 7, 273–286.

Lam, P.S., Freund, L.B., 1985. Analysis of dynamic growth of a tensile crack in elastic–plastic material. Journal of the Mechanics and Physics of Solids 33, 253–267.

Lee, Y.J., Freund, L.B. 1990. Fracture initiation due to asymmetric impact loading of an edge cracked plate. Journal of Applied Mechanics 57, 104–111.

Levy, A.J., 1994. Separation at a circular interface under biaxial load. Journal of the Mechanics and Physics of Solids 42, 1087–1104.

Mataga, P.A., Freund, L.B., Hutchinson, J.W., 1987. Crack tip plasticity in dynamic fracture. Journal of Physics and Chemistry of Solids 48, 985–1005.

Mello, M.C., Prakash, V., Clifton, R.J., 1991. Multi-point interferometry for monitoring two-dimensional wave motions, in shock compression of condensed matter. Proceedings of the American Physical Society Topical Conference. Williamsburg, VA, pp. 763–767.

Moran, J., Shih, C.H., 1987. General treatment of crack tip contour integrals. International Journal of Fracture 35, 295–310.

Nakamura, T., Shih, C.F., Freund, L.B., 1985. Computational methods based on an energy integral in dynamic fracture. International Journal of Fracture 27, 229–243.

Nagtegaal, J.C., Parks, D.M., Rice, J.R., 1974. On numerically accurate finite element solutions in the fully plastic range. Computer Methods in Applied Mechanics and Engineering 4, 153–175.

Needleman, A., 1985. On finite element formulation for large elastic–plastic deformations. Computers and Structures 20, 247–257.

Needleman, A., 1987. A continuum model for void nucleation by inclusion debonding. Journal of Applied Mechanics 54, 525–531.

Needleman, A., 1990a. An analysis of decohesion along an imperfect interface. International Journal of Fracture 42, 21–40.

Needleman, A., 1990b. An analysis of tensile decohesion along the interface. Journal of the Mechanics and Physics of Solids 38, 289–324.

Needleman, A., Tvergaard, V., 1991. Analysis of dynamic, ductile crack growth in a double edge cracked specimen. International Journal of Fracture 49, 41–67.

Pierce, D., Shih, C.F., Needleman, A., 1984. A tangent modulus method for rate dependent solids. Computers and Structures 18, 875–887.

Povrik, G.L., Needleman, A., Nutt, S.R., 1990. An analysis of residual stress in whisker-reinforced Al–SiC composites. Material Science and Engineering A125, 129–140.

Prakash, V., 1993. Plate impact investigations of dynamic fracture and time resolved friction. Ph. D. thesis, Brown University, Province, Rhode Island, U.S.A.

Prakash, V., Clifton, R.J., 1992. Experimental and analytical investigations of dynamic fracture under conditions of plane strain. In: Ernst, H.A., Saxena, A., Dowell, D.L. (Eds.), Proceedings of 22nd Material Symposium of Fracture Mechanics 1, ASTM STP 1131. Philadelphia, pp. 412–444.

Premack, T., Douglas, A.S., 1995. Three-dimensional analysis of impact fracture of 4340VAR steel. International Journal of Solids and Structures, Vol. 32 (17/18) 2793–2812.

Ravichandran, G., 1983. A plate impact experiment for studying crack initiation at loading rates $\dot{K}_I \approx 10^8$ MPa$\sqrt{\text{m}}$/s. Sc.M. thesis, Brown University, Providence, Rhode Island, U.S.A.

Ravichandran, G., Clifton, R.J., 1989. Dynamic fracture under plane wave loading. International Journal of Fracture 40, 157–201.

Rice, J.R., 1968. A path independent integral and the approximate analysis of strain concentration by notches and cracks. Journal of Applied Mechanics 35, 379–386.

Rosakis, A.J., Zhender, A.T., 1990. Dynamic fracture initiation and propagation in 4340 steel under impact loading. International Journal of Fracture 43, 271–285.

Rosakis, A.J., Duffy, J., Freund, L.B., 1984. The determinism of dynamic fracture toughness of AISI 4340 steel by the shadow spot method. Journal of the Mechanics and Physics of Solids 32, 443–460.

Rose, J.H., Ferrante, J., Smith, J.R., 1981. Universal binding energy curves for metals and bimetallic interfaces. Physics Review Letters 47, 675–678.

Siegmund, T., Needleman, A., 1997. A numerical study of dynamic crack growth in elastic– viscoplastic solids. International Journal of Solids and Structures 34, 769–785.

Suo, Z., Ortiz, M., Needleman, A., 1992. Stability of solids with interfaces. Journal of the Mechanics and Physics of Solids 40, 613–640.

Taylor, G.I., Quinney, H., 1934. The latent energy remaining in a metal after cold working. Proceedings of the Royal Society of London A143, 307–326.

Tvergaard, V., 1982. Influence of void nucleation on ductile shear fracture at a free surface. Journal of the Mechanics and Physics of Solids 30, 399–425.

Tvergaard, V., Hutchinson, J.W., 1993. The influence of plasticity on mixed mode interface toughness. Journal of the Mechanics and Physics of Solids 41, 1119–1135.

Tvergaard, V., Hutchinson, J.W., 1992. The relation between crack growth resistance and fracture process parameters in elastic–plastic solids. Journal of the Mechanics and Physics of Solids 40, 1377–1392.

Tvergaard, V., Needleman, A., 1993. An analysis of the brittle–ductile transition in dynamic crack growth. International Journal of Fracture 59, 53–67.

Varias, A.G., Shih, C.F., 1993. Quasi-static crack advance under a range of constraints—steady state fields based on a characteristic length. Journal of the Mechanics and Physics of Solids 41, 835–856.

Xu, X.P., Needleman, A., 1993. Void nucleation by inclusion debonding in a crystal matrix. Modeling Simulations in Material Science and Engineering 1, 111–132.

Xu, X.P., Needleman, A., 1994. Numerical simulations of fast crack growth in brittle solids. Journal of the Mechanics and Physics of Solids 42, 1397–1434.